EDITOR
Prof. Dr. Çoşkun ÖZALP

Research and
Evaluations in the Field of

ENGINEERING

June 2025

Privilege Holder • Yaşar Hız
Editor-in-chief • Eda Altunel
Prepared for Publication • Gece Kitaplığı
Editor • Prof. Dr. Çoşkun ÖZALP

First Edition • June 2025 / ANKARA

ISBN • 978-625-388-435-2

Gece Kitaplığı
Adress: Kızılay Mah. Fevzi Çakmak 1. Sokak Ümit Apt
No: 22/A Çankaya/ANKARA Tel: 0312 384 80 40

www.gecekitapligi.com
gecekitapligi@gmail.com

Printing and Binding
Bizim Buro
Certificate No: 42488

Research And Evaluations In The Field Of Engineering

June 2025

Editor:
Prof. Dr. Çoşkun ÖZALP

CONTENTS

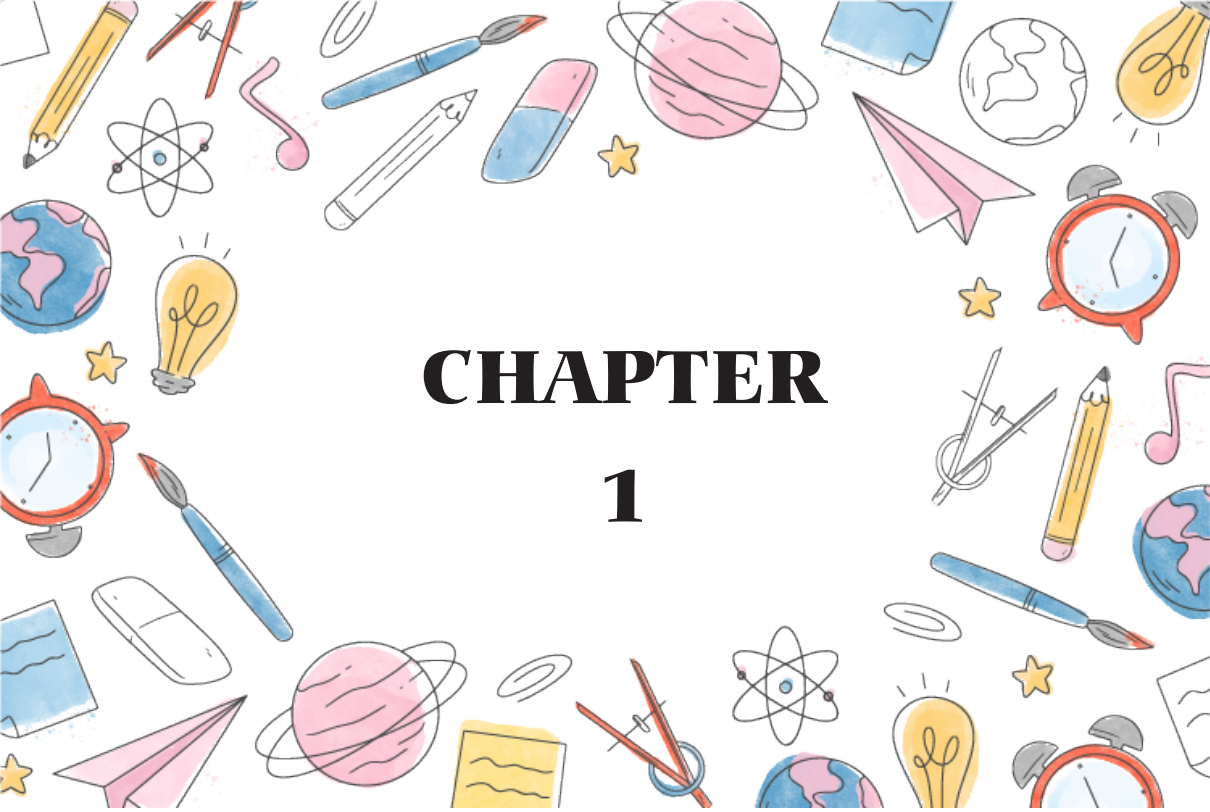

CHAPTER 1

ADVANCED CLAY-BASED PROTECTIVE COATINGS FOR AUTOMOTIVE APPLICATIONS

Tarık Eren BOYLU[1]

Nil ACARALI[2]

1 Yildiz Technical University, Department of Chemical Engineering, 34220, Esenler-Istanbul, Türkiye., ORCID: 0009-0008-8883-0995

2 Yildiz Technical University, Department of Chemical Engineering, 34220, Esenler-Istanbul, Türkiye., ORCID: 0000-0003-4618-1540

1. INTRODUCTION

The automotive industry was currently navigating a critical transitional phase, where it could balance technological advancements with environmental obligations and increasing consumer demands for durability and high performance. Automotive coatings, which protected vehicle surfaces and enhance their visual appeal, played a key role in preserving structural integrity, resisting environmental degradation, and extending the lifespan of automotive components. Traditionally, these coatings had relied heavily on synthetic, petroleum-derived materials such as epoxy resins and polyurethane systems [1]. While these conventional materials were effective in providing mechanical strength and corrosion resistance, they pose significant environmental challenges. High emissions of volatile organic compounds (VOCs), energy-intensive production processes, and limited recyclability were major contributors to ecological impact [2].

The exploration of innovative materials that combined environmental sustainability with high-performance capabilities became a growing area of interest [3]. Clays such as zeolite, montmorillonite, sepiolite, and halloysite possess layered structures that could be modified or functionalized to improve compatibility with polymer matrices, making them suitable additives for automotive coatings [4]. These materials offered a range of advantageous properties, including thermal stability, hydrophobicity, corrosion resistance, and mechanical reinforcement—features that were crucial for both exterior and interior automotive applications [5]. Unlike traditional coatings that often relied on heavy metal pigments or toxic solvents, clay-based alternatives present an opportunity to reduce environmental impact while maintaining—or even exceeding—the performance standards set by conventional systems [6]. This dual advantage positioned clay-derived materials as a key component in the next generation of automotive coatings, capable of meeting the evolving demands of the industry. Figure 1 illustrated the multi-layer structure of automotive coatings, each contributing specific protective and aesthetic functions to enhance the vehicle's durability and appearance.

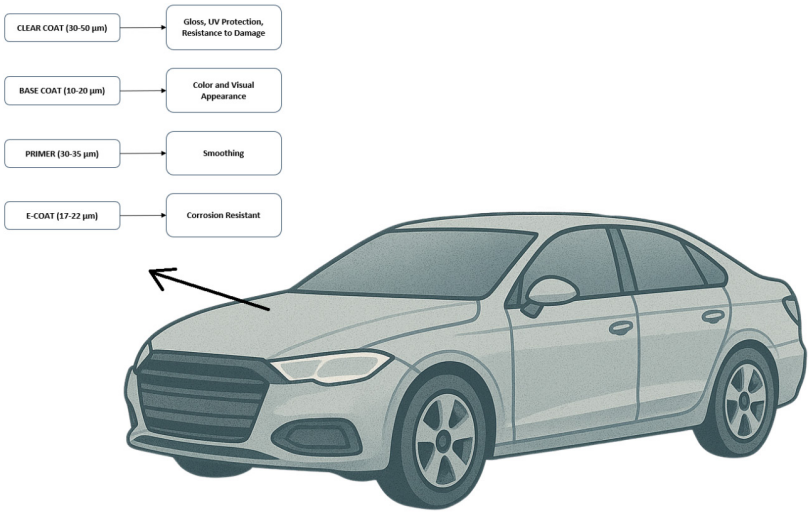

Figure 1. *Layers of Automotive Coatings*

The motivation behind this chapter from the necessity to mitigate the environmental drawbacked associated with conventional automotive coatings. For instance, traditional epoxy-based coatings—valued for their robustness—typically required energy-intensive curing processes and emit volatile organic compounds (VOCs), contributing to air pollution [7]. Similarly, protective layers containing metals such as chromium or nickel raise concerned related to toxicity and disposal challenges [8]. In contrast, clay-derived materials offered a sustainable pathway to enhancing coating performance by leveraging inherent properties such as high surface area, ion exchange capacity, and thermal resistance—without compromising ecological integrity [9]. Recent advancements in nanotechnology had further expanded the potential of these materials, enabling the development of nanocomposites with superior mechanical strength and barrier properties through nanoscale clay integration [10].

The significance of automotive coatings extended beyond surface protection; they also played a vital role in vehicle aesthetics, safety, and overall operational efficiency [11]. Meeting these diverse requirements demanded a careful balance of material properties—one that clay-based systems were uniquely positioned to offer. For instance, the incorporation of montmorillonite into epoxy matrices could significantly enhance corrosion resistance under acidic conditions [12], while halloysite nanoclay imparts superhydrophobic characteristics that prevented water retention and ice formation [13].

The literature highlighted a growing research field focused on enhancing coating performance using clay-based materials and nanocomposites. Epoxy-based coatings, a fundamental material in industrial applications, had been extensively modified with inorganic fillers such as organically modified sepiolite (OMSEP) and attapulgite (ATP) to improve corrosion resistance and mechanical properties. Studies demonstrated that adding just 3% OMSEP significantly enhances coating performance while reducing production costs, underscoring the economic viability of these approaches [14]. Similarly, superhydrophobic coatings based on ATP clay modified with hexadecyltrimethoxysilane (HDTMS) gained attention for their self-cleaning capabilities and durability, proving suitability for industrial-scale applications [15]. Beyond epoxies, siloxane-based systems and biocomposites containing natural fibers and nanoclays offered high corrosion resistance and thermal stability, expanding the scope of sustainable coating technologies [16].

A notable trend in the field is the development of hybrid systems in which clay was combined with other advanced nanomaterials such as zinc oxide (ZnO), graphene oxide (GO), or metal-organic frameworks (MOFs), yielding synergistic effects. For instance, bentonite/ZnO/CuO nanocomposites demonstrated remarkable photocatalytic activity capable of degrading surface pollutants on vehicle bodies [1], while ZnO/GO/montmorillonite hybrids exhibited enhanced oxygen barrier properties and antibacterial functionality [10]. These innovations underscored the versatility of clay-based materials and their potential to address a wide spectrum of automotive challenges—from corrosion protection to environmental self-regulation. Furthermore, the integration of intelligent functionalities such as pH-responsive corrosion inhibition or self-healing mechanisms into clay-enhanced coatings pushed the boundaries of coating technology and promises improved durability under the extreme service conditions encountered in automotive environments [17].

Despite these advancements, significant gaps remained in translating laboratory-scale successes to industrial applications [18]. Moreover, the long-term performance of these materials—under environmental stressors like prolonged exposure to saltwater, high humidity, or mechanical wear—could be rigorously validated through experimental testing [8]. Stress analyses were essential to ensure coatings could withstand the dynamic conditions of automotive operations, from urban transport to off-road applications. Additionally, the environmental benefits of clay-derived materials—such as reduced energy consumption during production and lower VOC emissions—could be quantitatively assessed through life cycle analyses to substantiate sustainability claims [11].

This chapter aimed to systematically evaluate the potential of clay-based materials in automotive coatings to address existing challenges. The primary objective was to assess their feasibility as eco-friendly alternatives that met the stringent performance requirements of the automotive industry. Focusing on key properties such as thermal resistance, water repellency, corrosion resistance, and mechanical durability, this chapter sought to comprehensively understand how clay additives could enhance coating performance [12].

The broader implications of this chapter lied in its potential to transform the automotive coating landscape. By reducing reliance on environmentally harmful materials and processes, clay-based coatings could contribute to a more sustainable automotive industry, aligning with global efforts to combat climate change and resource scarcity [11]. For instance, adopting these materials could lower the ecological footprint of vehicle production, which was responsible for significant carbon emissions and material waste. Furthermore, the enhanced durability offered by clay-enhanced coatings could reduce maintenance costs for both consumers and manufacturers, providing economic incentives alongside environmental benefits [19]. This dual focused on performance and sustainability positions the research at the intersection of technological innovation and ecological responsibility, offering a roadmap for future advancements in automotive materials.

The structure of this chapter was designed to provide a comprehensive review of clay-derived coatings in the automotive context. Following the introduction, the literature review synthesized existing studies on clay-based and nanocomposite coatings, highlighting their strengths and limitations [2, 7].

In summary, the development of eco-friendly, sustainable, and high-performance automotive coatings represented a critical step toward aligning the demands of modern transportation with environmental responsibility. With inherent versatility and eco-friendly profile, clay-derived materials offered a robust solution to this challenge [3]. As the industry shifts toward greener technologies, the insights could serve as a catalyst for the broader adoption of sustainable materials, reshaping the future of automotive manufacturing and beyond.

2. COATINGS

2.1. Epoxy-Based Coatings and Clay Modifications

Epoxy-based coatings were renowned for durability and corrosion resistance in automotive and industrial applications; however, enhancing

properties often required modification with clay-derived materials. NiCrAl-bentonite-based coatings provided effective protection against thermal and salt corrosion in marine environments but tended to degrade under harsh NaCl-containing conditions due to chlorination and oxidation [8]. To overcome such limitations, the integration of inorganic nanofillers like organically modified sepiolite (OMSEP) into epoxy coatings had been proposed; adding just 3% OMSEP enhances corrosion resistance while reducing production costs [14]. Similarly, siloxane-based epoxy coatings, developed through cationic photopolymerization, offered superior corrosion protection, with variants like SAE-15 demonstrating high performance [16]. Another innovation in clay modification involved treating montmorillonite with zinc phosphate to protect steel surfaces in challenging environments like acid rain, enhancing inhibitor effectiveness [12]. In the transition to smart coating technologies, epoxy coatings containing a type of zeolites provided long-term corrosion protection for alloys, showing promise for automotive and aerospace applications [17]. Figure 2 showed the uniform dispersion of layered clay nanoparticles within a polymer matrix, illustrating how the nanofillers integrate with polymer chains to enhance mechanical strength, barrier properties, and thermal stability of nanocomposite coatings.

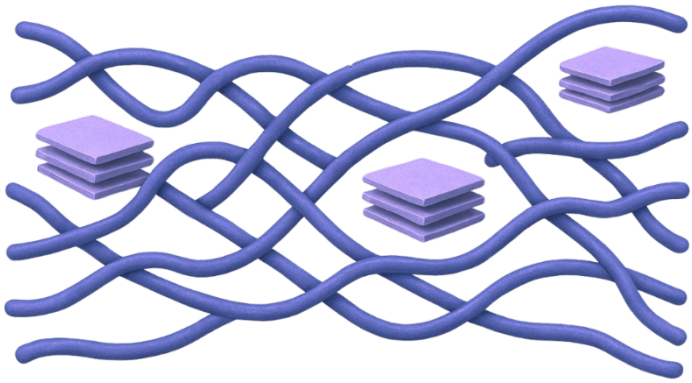

Figure 2. *Dispersion of clay nanoparticles in the polymer matrix*

By ensuring uniform dispersion inside the epoxy matrix, montmorillonite treated with zinc-based ionic liquids promotes its corrosion resistance and self-healing qualities [20]. In a more environmentally friendly approach, active montmorillonite nanofillers contribute to the development of non-toxic coatings [21]. The combination of silica aerogel and organic montmorillonite increases mechanical strength by 146% while sig-

nificantly reducing heat and smoke emissions [22]. Epoxy coatings enriched with MOF and graphene oxide (GO) enhance thermal and mechanical properties, advancing innovations in this field [23]. Coatings developed with halloysite and fluoro-polysilsesquioxane reduce friction and enhance hydrophobicity [24]. Finally, loading halloysite nanotubes with benzotriazole imparted long-term corrosion protection and self-healing capabilities to epoxy coatings [25].

2.2. Hydrophobic and Superhydrophobic Coatings

Hydrophobic and superhydrophobic coatings significantly enhanced the durability of automotive surfaces by repelling water and preventing dirt accumulation. Attapulgite (ATP)-based systems modified with hexadecyltrimethoxysilane (HDTMS) exhibited strong corrosion resistance and mechanical robustness when applied to aluminum alloys, making suitable for industrial-scale applications [15]. Similarly, halloysite nanoclay treated with polysiloxane created superhydrophobic surfaces on glass and carbon fiber composites, effectively reducing ice adhesion and enhancing vehicle safety in cold environments [13].

Alternative eco-friendly materials had also gained attention for hydrophobic surface modification. For example, carnauba wax-based particles synthesized through the Pickering emulsion method increased the water contact angle on chitosan-based films, providing a sustainable coating solution [26]. In another biomimetic strategy, polydopamine inspired by mussel adhesion was used to modify mica, significantly improving both hydrophobicity and thermal/mechanical properties in poly(lactic acid) coatings [27]. Additionally, mechanically activated $AlPO_4$ improved coating adhesion, enhances water resistance, and extended service life [28]. In polyurethane-based systems, the inclusion of clay enhanced thermal and mechanical resilience while strengthening the water barrier effect, thus offering a robust solution for demanding automotive environments [29].

2.3. Nanocomposite Coatings and Photocatalytic Applications

Nanocomposite coatings, leveraging the synergy of clay and other nanomaterials, offered innovative properties, with photocatalytic applications standing out in this field. Bentonite/ZnO/CuO nanocomposites exhibited high photocatalytic activity in removing pollutants like methylene blue, with the combination of ZnO and CuO enhancing dye degradation efficiency [1]. This synergistic effect was supported by studies improving the photocatalytic performance of hybrid systems [7]. The morphology of ZnO nanoparticles played a critical role in optimizing oxygen barrier and

antibacterial properties in ZnO/GO/MMT coatings, demonstrating the versatility of nanocomposites [10].

ZnO structures produced via thermal oxidation exhibit peak photocatalytic performance at 800°C, proving their applicability on steel surfaces [30]. Nano-carbon coatings, when combined with Ti_3C_2 and bentonite, reduced the Schottky barrier, enhancing photocatalytic activity and offering potential for wastewater treatment [31]. Dual-domain quarter-wave retarder technology mitigated reflective color differences, improving display clarity and providing an effective solution for enhancing the performance of automotive OLED displays [32].

2.4. Smart Coatings and Industrial Applications

Smart coatings offered innovative solutions for corrosion protection and industrial scalability. pH-responsive systems based on sepiolite and MOFs enhance the efficiency of epoxy matrices in harsh environments [2]. Epoxy based coatings incorporating a type of zeolites have demonstrated long-term protection of Mg-Li alloys, suggesting strong potential for applications in sectors such as automotive and aerospace [17].

Nanocontainers loaded with plant extracted and based on sepiolite provide environmentally friendly corrosion protection for steel surfaces via a pH-triggered controlled release mechanism [33]. Similarly, zeolite-based coatings exhibited self-healing behavior and were confirmed to be industrially viable through electrochemical impedance spectroscopy (EIS) analyses [34]. Dual-inhibitor-loaded ZIF-8 and montmorillonite nanocontainers maintained high impedance even after 28 days in salt spray testing, offering active corrosion resistance in epoxy systems [35]. In aerospace, PU/GCN-ABES/Ta_3N_5 nanocomposite coatings safeguarded aluminum alloys with superior hydrophobicity and corrosion resistance [36], while in automotive applications, PU-GCN-AAMS/MoN coatings stand out for their long-term durability against chloride ions and enhanced mechanical performance [37].

2.5. Biocomposites for Thermal and Mechanical Durability

Biocomposites leveraged natural materials to enhance thermal and mechanical durability. Sunn hemp fibers and nanoclay-reinforced polyester nanocomposites reduced water absorption, thereby improving durability for automotive applications [19].

YAG bond coatings had been found to offer higher adhesion strength compared to Zn bond coatings, enhancing bonding through mechanical interlocking with carbon fibers. This study demonstrated the effectiveness of

YAG coatings in improving the performance of thermally sprayed coatings [38]. Transverse cracks were observed in ceramic coatings under thermal load, with an increase in elastic modulus lowering the damage initiation temperature. Differences in thermal expansion coefficients were identified as having a significant impact on coating durability [39]. Bio-based benzoxazine and epoxidized castor oil copolymers introduced innovation in coatings with rapid thermo-responsive self-healing properties [40]. Chitosan and chitosan Schiff base biocomposites enhanced corrosion resistance on copper surfaces in saline environments, with the effect further amplified by strontium titanate nanoparticles [41]. These studies highlighted that biocomposites offer environmentally friendly and functional solutions.

2.6. Flame-Retardant Coatings and Nanocomposites

Flame-retardant coatings were critical for safety and durability. Bentonite and montmorillonite-based multilayer nanocomposites reduced burning rates, enhance char yield, and provided high flame retardancy [5].

Functionalized halloysite nanotubes bolster fire resistance was playing a complementary role in this domain [42]. The combination of graphene oxide and montmorillonite improved thermal stability and adhesion properties in epoxy nanocomposites offering a sustainable flame-retardant solution [43]. Bio-based phytic acid and urea-modified montmorillonite integrated impact resistance and flame retardancy in polyurea coatings [44]. Thermal barrier coatings, through optimized coating thickness, reduced delamination forces and ensure durability under thermo-mechanical loads [45]. These systems demonstrated the effectiveness of nanocomposites in flame retardancy.

2.7. Environmental Sustainability and Future Perspectives

Environmental sustainability was becoming increasingly significant in coating technologies. Life cycle assessments of mycelium-based composite panels revealed that energy consumption during production determined environmental impact, guiding future design strategies [11].

Zeolite/polyurea coatings contributed to building energy efficiency through high solar reflectivity and UV resistance [46]. Protective coatings in automotive, aerospace, and military applications offered eco-friendly solutions while highlighting the need for further research into smart coatings [47]. Thermal spray techniques provided low porosity and strong adhesion in functional and smart coatings, laying the groundwork for future innovations [48]. Interactions between photoreactive stabilizers and UV absorbers, such as HALS 1, extended the environmental lifespan of coatings by

creating synergistic effects [49]. These studies underscored the integration of sustainability and technological advancement, shaping future research directions.

3. CONCLUSION

The chapter systematically demonstrated the potential of clay-based materials as environmentally friendly, sustainable, and high-performance alternatives in automotive coatings. Clays such as bentonite, montmorillonite, and sepiolite, when incorporated into epoxy and polyurethane matrices, offered significant improvements in key properties including thermal resistance, hydrophobicity, corrosion protection, and mechanical strength. Furthermore, these materials helped reduce volatile organic compound (VOC) emissions and energy consumption during production, aligning with the ecological goals of the automotive industry. With the aid of nanotechnology, advanced clay-based nanocomposites had been developed that delivered innovative functionalities such as photocatalytic activity and self-healing behavior, taking coating performance to a higher level.

The chapter also assessed the chemical compatibility and performance of these materials under various conditions but acknowledged the need for further experimental validation to support their industrial-scale application. Additionally, overcoming challenges related to scalability and cost-efficiency in manufacturing was crucial for widespread adoption. Clay-derived materials not only meet or exceed traditional performance standards but also contributed to global efforts aimed at reducing the automotive sector's environmental footprint. In this regard, the study standed as a bridge between technological innovation and environmental responsibility, offering a promising step toward greener and more resilient coating solutions for the future.

REFERENCES

[1] Długosz, O., Wąsowicz, N., Szostak, K., & Banach, M. (2021). Photocatalytic properties of coating materials enriched with bentonite/ZnO/CuO nanocomposite. *Materials Chemistry and Physics*, 260, 124150. https://doi.org/10.1016/j.matchemphys.2020.124150

[2] Chen, H., Yu, Z., Yang, G., Liao, K., Peng, B., Pang, Y., Zhu, L., & Tang, J. (2022). A novel pH-responsive smart anticorrosion coating based on sepiolite and MOF for high-performance corrosion protection. *Surface & Coatings Technology*, 446, 128768. https://doi.org/10.1016/j.surfcoat.2022.128768

[3] Vega, J. M., Granizo, N., Simancas, J., Díaz, I., Morcillo, M., & de la Fuente, D. (2017). Exploring the corrosion inhibition of aluminium by coatings formulated with calcium exchange bentonite. *Progress in Organic Coatings,* 111, 273-282. https://doi.org/10.1016/j.porgcoat.2017.06.001

[4] Wang, S., Huang, R., Ren, K., Shen, L., Li, X., Lei, G., Shen, L., Zhan, Y., Zheng, Y., & Jiang, L. (2023). Structural control of PEG-intercalating Na-bentonite and its influence on the properties of castor oil-based polyurethane coating. *Progress in Organic Coatings,* 178, 107499. https://doi.org/10.1016/j.porgcoat.2023.107499

[5] Lee, I., Kim, S.J., Byun, Y.Y., Chang, I., Ju, Y.W., Park, Y. T., Jang, J., & Cho, C. (2023). High flame retardancy enabled by dual clays-based multilayer nanocomposites. *Progress in Organic Coatings,* 183, 107784. https://doi.org/10.1016/j.porgcoat.2023.107784

[6] Yatika, G., Ram Kumar, S., Patel, P. B., Singh, D.P., Rajkamal, M.D., & Boopathi, S. (Article in press). Experimental investigation of RHA biochar and tamarind fibre epoxy composite. *Materials Today: Proceedings*. https://doi.org/10.1016/j.matpr.2023.02.439

[7] Khosrowshahi, M.S., Hariri, S.A., Rahimi, M., Emrooz, H.B.M., & Shemirani, F. (2024). Green synthesis of a ZnO/ZnS-decorated magnetic porous carbon hybrid for enhanced rhodamine B adsorption and photodegradation: A combined DFT and experimental study. *Sustainable Materials and Technologies*, e01231. https://doi.org/10.1016/j.susmat.2024.e01231

[8] Chen, L., Sun, Z.R., Li, C.J., & Yang, G.J. (2024). Response of NiCrAl-bentonite abradable seal coatings to thermal/salt corrosion. *Corrosion Science*, 233, 112111. https://doi.org/10.1016/j.corsci.2024.112111

[9] Zhang, N., Zhou, B., Liu, Y., Yang, B., Zheng, H., & Wu, Y. (2023). Dual-functional anti-corrosion coatings with surface hydrophobicity and internal smart-releasing Ce^{3+} loaded in bentonite on carbon steel. *Journal of Materials Research and Technology*, 22, 879-894. https://doi.org/10.1016/j.jmrt.2022.11.127

[10] Alp, E., Olivieri, F., Aulitto, M., Castaldo, R., Contursi, P., Cocca, M., & Gentile, G. (2024). The effect of ZnO nanoparticles morphology on the barrier

and antibacterial properties of hybrid ZnO/graphene oxide/montmorillonite coatings for flexible packaging. *Surfaces and Interfaces*, 55, 105307. https://doi.org/10.1016/j.surfin.2024.105307

[11] Weinland, F., Lingner, T., Schritt, H., Gradl, D., Reintjes, N., & Schüler, M. (2024). Life cycle assessment of mycelium based composite acoustic insulation panels. *Cleaner and Circular Bioeconomy,* 9, 100106. https://doi.org/10.1016/j.clcb.2024.100106

[12] Korniy, S., Danyliak, M.O., & Lavrys, S. (2025). Preparation and properties of modified montmorillonite by zinc-phosphate for anticorrosion applications in protective coatings. *Materials Chemistry and Physics*, 335, 130537. https://doi.org/10.1016/j.matchemphys.2025.130537

[13] Kaybal, H.B., Duzcukoglu, H., & Asmatulu, R. (2025). Integration of polysiloxane-modified halloysite nanoclay nanocomposite coatings on fiber-reinforced polymeric composites structures: Part II—Icing/deicing, self-cleaning, sandpaper abrasion, and water immersion performances. *Composites Part A: Applied Science and Manufacturing*, 193, 108879. https://doi.org/10.1016/j.compositesa.2025.108879

[14] Xiong, H., Qi, F., Zhao, N., Yuan, H., Wan, P., Liao, B., & Ouyang, X. (2020). Effect of organically modified sepiolite as inorganic nanofiller on the anti-corrosion resistance of epoxy coating. *Materials Letters*, 260, 126941. https://doi.org/10.1016/j.matlet.2019.126941

[15] Liu, X., Zhan, T., & Zhang, B. (2024). Attapulgite-based superhydrophobic coating on aluminum alloy substrate with self-cleaning, anti-corrosion and robustness. *Journal of Industrial and Engineering Chemistry*, 130, 357-367. https://doi.org/10.1016/j.jiec.2023.09.039

[16] Liao, F.Q., & Chen, Y.C. (2023). Siloxane-based epoxy coatings through cationic photopolymerization for corrosion protection. *Progress in Organic Coatings*, 174, 107235. https://doi.org/10.1016/j.porgcoat.2022.107235

[17] Wang, Y., Zhu, Y., Li, C., Song, D., Zhang, T., Zheng, X., Yan, Y., Zhang, M., Wang, J., & Shchukin, D.G. (2016). Smart epoxy coating containing Ce-MCM-22 zeolites for corrosion protection of Mg-Li alloy. *Applied Surface Science,* 369, 384–389. https://doi.org/10.1016/j.apsusc.2016.02.102

[18] Zhang, Q., Shu, Y., Zhang, Y., Huo, S., Ye, G., Wang, C., & Liu, Z. (2024). Effect of functionalized halloysite nanotubes on fire resistance and water tolerance of intumescent fire-retardant coatings for steel structures. *Progress in Organic Coatings*, 197, 108843. https://doi.org/10.1016/j.porgcoat.2024.108843

[19] Arumugam, G.S., Arumugam, C., Damodharan, K., Kumar, R.S., Gummadi, S.N., & Muthusamy, S. (2024). Thermal and mechanical properties of high-performance polyester nanobiocomposites reinforced with pre-treated sunn hemp fiber for automotive applications. *International Journal of Biological Macromolecules*, 280, 135591. https://doi.org/10.1016/j.ijbiomac.2024.135591

[20] Henriques, R.R., Carelo, J.C., & Soares, B.G. (2024). Anti-corrosive and self-healing properties of epoxy coatings loaded with montmorillonite modified with zinc-based ionic liquid. *Progress in Organic Coatings,* 187, 108185. https://doi.org/10.1016/j.porgcoat.2023.108185

[21] Li, X., Shao, Y., Wang, Y., & Wang, J. (2025). Eco-friendly design of active montmorillonite nanofillers for reinforcing the anti-corrosion property of epoxy coating. *Applied Clay Science,* 267, 107739. https://doi.org/10.1016/j.clay.2025.107739

[22] Liu, Y.W., Nong, Z.S., Man, T.N., Lu, S.W., & Dong, L.H. (2024). SiO_2 aerogel coating with organic montmorillonite compounded with flame retardants: A strategy for design of a multifunctional thermal barrier coating. *Journal of Materials Research and Technology,* 30, 318–331. https://doi.org/10.1016/j.jmrt.2024.03.083

[23] Haeri, Z., Ramezanzadeh, B., & Ramezanzadeh, M. (2022). Recent progress on the metal-organic frameworks decorated graphene oxide (MOFs-GO) nano-building application for epoxy coating mechanical-thermal/flame-retardant and anti-corrosion features improvement. *Progress in Organic Coatings,* 163, 106645. https://doi.org/10.1016/j.porgcoat.2021.106645

[24] Frías Gallardo, L., Montemartini, P.E., & Penoff, M.E. (2023). Enhanced slurry erosion resistance of low friction and highly hydrophobic halloysite-fluoro-polysilsesquioxane coatings. *Wear*, 526-527, 204875. https://doi.org/10.1016/j.wear.2023.204875

[25] Yang, T., Wang, T., Feng, H., Chen, B., Cao, L., Sun, T., Li, W., & Chen, S. (2024). Construction of smart halloysite nanocontainers for active long-term anticorrosion of epoxy coatings. *Progress in Organic Coatings,* 187, 108146. https://doi.org/10.1016/j.porgcoat.2023.108146

[26] Zhang, N., Gao, C., Meng, L., & Tang, X. (2023). Preparation and characterization of carnauba wax-based particle with hierarchical structure and its use as hydrophobic coating for chitosan films. *Carbohydrate Polymers,* 319, 121224. https://doi.org/10.1016/j.carbpol.2023.121224

[27] Wei, X.Y., Li, W., Li, J., & Niu, X.T. (2024). Mussel-inspired polydopamine modified mica with enhanced mechanical strength and thermal performance of poly(lactic acid) coating. *International Journal of Biological Macromolecules,* 273(Part 2), 133148. https://doi.org/10.1016/j.ijbiomac.2024.133148

[28] Li, M., Zhou, X., Zhao, J., Hong, Y., Qu, S., & Wang, P. (2023). Enhancing the adhesive strength of solar reflective coatings via mechanical activation. *Powder Technology,* 422, 118433. https://doi.org/10.1016/j.powtec.2023.118433

[29] Babar, M., Kaur, L., & Verma, G. (2025). Evaluation of clay loaded polyurethane nanocomposite coatings for thermal, mechanical and water barrier performance. *Surfaces and Interfaces,* 58, 105810. https://doi.org/10.1016/j.surfin.2024.105810

[30] Dikici, T. (2017). Temperature-dependent growth of ZnO structures by thermal oxidation of Zn coatings electrodeposited on steel substrates and their photocatalytic activities. *Ceramics International,* 43(11), 8289–8293. https://doi.org/10.1016/j.ceramint.2017.03.162

[31] Wang, L., Liu, K., Fu, T., Sun, J., Yan, J., Hu, Y., Tong, Z., & Zhang, H. (2024). Multiple effects of nano-carbon coating on mediating Schottky barrier height, inhibiting Ti_3C_2 oxidation and elevating photocatalytic activity in BiOBr/carbon-coated Ti_3C_2/exfoliated bentonite. Chemical Engineering Journal, 480, 148252. https://doi.org/10.1016/j.cej.2023.148252

[32] Choi, T.H., Baek, J.M., Lee, H.W., & Ha, J.U. (2022). Elimination of ambient light reflection color in automotive organic light emitting diode displays. *Optical Materials,* 134, 113173. https://doi.org/10.1016/j.optmat.2022.113173

[33] Zarki, Y., Elmourabit, M., Ben Seddik, N., Akachar, S., Achache, M., Oulad Idriss, H., Chaouket, F., Draoui, K., & AitAghzzaf, A. (2024). Grafted sepiolite as smart nanocontainer for *Daphne Gnidium* plant extract: pH-dependent controlled release and effective green anti-corrosion coating. *Surfaces and Interfaces,* 51, 104754. https://doi.org/10.1016/j.surfin.2024.104754

[34] Tamilvanan, S., Balasubramaniam, S., & Ramadoss, A. (2024). Dual templated-based synthesis of smart zeolites and its self-healing anticorrosion coatings. *European Polymer Journal*, 210, 112957. https://doi.org/10.1016/j.eurpolymj.2024.112957

[35] Wang, C., Zhao, C., Li, Y., Yuan, W., Huang, Y., Cheng, D., Shen, T., Zhang, J., Liu, J., Jiang, L., Yang, C., Shen, Q., & Yang, H. (2025). Application of dual inhibitor-loaded ZIF-8 decorated montmorillonite nanocomposite toward active corrosion resistance of waterborne epoxy coatings. *Applied Surface Science,* 697, 163021. https://doi.org/10.1016/j.apsusc.2025.163021

[36] Xavier, J.R., & Vinodhini, S.P. (2024). Advanced nanocomposite coating for aluminium alloy with enhanced corrosion resistance, flame retardancy, and mechanical strength in aircraft manufacturing industries. *Colloids and Surfaces A: Physicochemical and Engineering Aspects,* 698, 134543. https://doi.org/10.1016/j.colsurfa.2024.134543

[37] Xavier, J.R., & Vinodhini, S.P. (2024). Multifunctional nanocomposite coating for aluminium alloy: Corrosion resistance, flame retardancy, and mechanical enhancement for automotive components. *Materials Chemistry and Physics,* 323, 129628. https://doi.org/10.1016/j.matchemphys.2024.129628

[38] Pradhan, S.K., Kwon, E.P., Kweon, L.J., & Oh, M.S. (2024). Adhesion strength improvement of thermally sprayed metallic coating on carbon-fiber-reinforced polymer composite. *Materials Today Communications,* 41, 110619. https://doi.org/10.1016/j.mtcomm.2024.110619

[39] Wang, H., & Liang, L. (2024). Size effects on damage evolution of ceramic coatings under thermal loading. *Ceramics International,* 50(8), 12975–12984. https://doi.org/10.1016/j.ceramint.2024.01.207

[40] Mora, P., Rimdusit, S., & Jubsilp, C. (2024). Fast thermo-responsive thermoset self-healing polymers based on bio-derived benzoxazine/epoxidized castor oil copolymers for coating applications. *Arabian Journal of Chemistry,* 17(10), 106005. https://doi.org/10.1016/j.arabjc.2024.106005

[41] El Mahamdi, M., Daoudi, W., Naguib, I.A., Benhadi, L., Dagdag, O., Berisha, A., Kim, H., Noureddine, B., & El Aatiaoui, A. (2024). Enhanced corrosion protection of copper in saline environments using bio-nanocomposite coatings based on chitosan and chitosan Schiff base. *International Journal of Biological Macromolecules,* 282 (Part 6), 136702. https://doi.org/10.1016/j.ijbiomac.2024.136702

[42] Zhang, Q., Shu, Y., Zhang, Y., Huo, S., Ye, G., Wang, C., & Liu, Z. (2024). Effect of functionalized halloysite nanotubes on fire resistance and water tolerance of intumescent fire-retardant coatings for steel structures. *Progress in Organic Coatings,* 197, 108843. https://doi.org/10.1016/j.porgcoat.2024.108843

[43] Kabeb, S.M., Hassan, A., Mohamad, Z., Sharer, Z., Mokhtar, M., & Ahmad, F. (2022). Sustainable flame-retardant coating-based graphene oxide and montmorillonite. *Materials Today: Proceedings,* 51(Part 2), 1327–1331. https://doi.org/10.1016/j.matpr.2021.11.140

[44] Han, S., Li, S., Zhang, X., Liu, D., Guo, S., Wang, B., & Meng, Q. (2024). Enhancing the protective performance of anti-impact, corrosion resistant and flame retardant polyurea coatings using bio-based supramolecular decorated montmorillonite. *Construction and Building Materials,* 435, 136721. https://doi.org/10.1016/j.conbuildmat.2024.136721

[45] Li, L., & Zhang, W. (2022). Thickness effects on the delamination energy release rate of thermal barrier coating subjected to thermo-mechanical loads. *International Journal of Solids and Structures*, 254–255, 111937. https://doi.org/10.1016/j.ijsolstr.2022.111937

[46] Yang, S., Lei, S., Wang, F., Long, H., Ou, J., Amirfazli, A., & Baldelli, A. (2024). A comprehensive investigation of zeolite/polyurea cooling coating on concrete for building energy conservation. *Progress in Organic Coatings,* 188, 108265. https://doi.org/10.1016/j.porgcoat.2024.108265

[47] Makhlouf, A.S.H. (2014). Protective coatings for automotive, aerospace and military applications: Current prospects and future trends. In A. S. H. Makhlouf (Ed.), *Handbook of smart coatings for materials protection* (pp. 121–131). Woodhead Publishing. https://doi.org/10.1533/9780857096883.1.121

[48] Tejero-Martin, D., Rezvani Rad, M., McDonald, A., & Hussain, T. (2019). Beyond traditional coatings: A review on thermal-sprayed functional and smart coatings. *Journal of Thermal Spray Technology,* 28, 598–644. https://doi.org/10.1007/s11666-019-00857-1

[49] Ávár, L., & Bechtold, K. (1999). Studies on the interaction of photoreactive light stabilizers and UV-absorbers. *Progress in Organic Coatings,* 35(1–4), 11–17. https://doi.org/10.1016/S0300-9440(99)00031-4

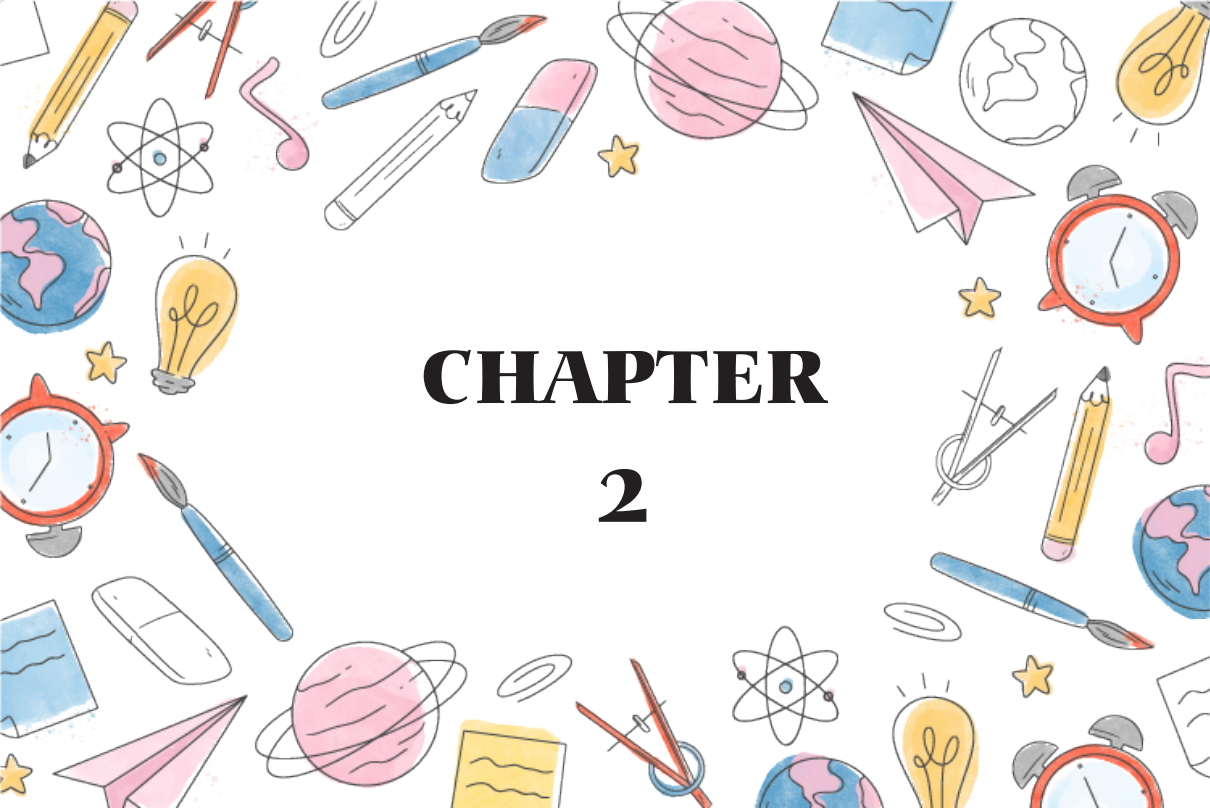

CHAPTER 2

WELD QUALITY ANALYSIS USING SIMULATION-BASED IMAGE PROCESSING APPROACHES

Adem DILBAZ[1]

Ilker Ali OZKAN[2]

1 Mechatronics Engineering, Institute of Sciences Selcuk University, Konya, Türkiye.

E-mail: adem.dilbaz@lisansustu.selcuk.edu.tr ORCID: 0000-0002-3135-7032

2 Department of Computer Engineering, Selcuk University, Konya, Türkiye.

E-mail: ilkerozkan@selcuk.edu.tr ORCID: 0000-0002-5715-1040

Introduction

Welding is the process of joining two or more materials under suitable physical and chemical conditions, with or without the use of additional materials of the same type. This practice contributes to maintaining the quality of the weld by ensuring that the materials are properly, firmly, and securely bonded to each other. However, if the protective material protecting the weld area against external factors is insufficient, the weld seam formed as a result of the joining process may become oxidized, brittle, and porous. In addition, improper adjustment of process parameters such as amperage, voltage, wire feed speed, welding feed speed, torch angle, and seam tracking points during the welding process can also lead to such problems. Factors that adversely affect weld quality can usually be determined relatively easily based on the observations of welding engineers and operators. In such relative determinations, the percentage of the amount of defects cannot be clearly determined, and some defects may be overlooked. There is an increasing trend in the use of image processing technologies, especially in the detection of gas and submerged arc welding defects, due to the advantage of higher sensitivity and less exposure to harsh environmental conditions [1]. In this context, the use of image processing-based technologies for more objective, reliable, and repeatable detection of welding defects has become an inevitable necessity.

Image processing technology enables the analysis of images captured by cameras, allowing desired findings to be automatically detected in artificial intelligence-based programs. In recent years, this vision-based technology has gained significant importance, particularly in industrial and scientific applications, due to its advanced optical features [2]. This data processing system utilizes images obtained from industrial, high-speed, thermal, color, and black-and-white camera systems for analysis. Consequently, various operations, such as object recognition and error detection, are performed, resulting in more effective and accurate outcomes. Cameras used as hardware are primarily classified into two main categories: CMOS (Complementary Metal-Oxide-Semiconductor) and CCD (Charge-Coupled Device). The visual data obtained by these image sensors are initially converted to a digital format. Following noise reduction, contrast enhancement, sharpening, thresholding, and gray level conversion, feature extraction for this data begins. Through this process, classification is completed for data with reduced dimensions, enhancing decision-making accuracy. In the field of image processing, integrating high-adaptability artificial intelligence algorithms with dynamic conditions offers more advantages over classical methods [3]. In robotic applications, these technologies are widely preferred, especially for detecting small defects that may occur in weld seams, as such minor issues can lead to significant structural failures

in the future [4]. In this context, integrating artificial intelligence approaches, such as fuzzy logic, artificial neural networks, and deep learning into image processing technologies allows for more sensitive, comprehensive, and reliable detection of weld defects in the digital environment [5].

Deep learning stands out as a powerful artificial intelligence-based method that can analyze various features in images by processing them in different layers, learn the relationships between these features, and automatically determine which information is more meaningful. Classical methods, on the other hand, lag behind deep learning-based approaches because feature extraction is defined manually, their accuracy rates are generally lower, and they do not allow the learned information to be reused in similar tasks. In this context, YOLO-based deep learning algorithms stand out with fewer parameters and higher inference speed in order to precisely detect even small defects such as surface cracks, internal cracks, and poor adhesion that may occur in welding processes [6].

In recent years, weld-related CAD models have been used in an integrated manner with various simulation programs, especially RoboDK [7]. This integration allows for testing image processing algorithms in virtual environments. Consequently, programs can be developed without the need for real field tests by utilizing RoboDK's camera interface with CAD models designed for welding defects. Additionally, advanced rendering settings in a simulation environment can enhance image quality in the data, allowing virtual weld defects to be visualized more realistically. All these possibilities provide significant advantages regarding measuring the accuracy of artificial intelligence-based algorithms and facilitating their integration into industrial processes. This chapter investigates how image processing and deep learning techniques can be employed for the automatic detection of weld defects; a simulation-supported system is proposed, and its performance is evaluated.

Image Processing Techniques

Image processing techniques are crucial in various domains, such as object recognition, error detection, and quality control in industrial applications. These techniques are generally examined in two main groups: traditional methods and AI-based techniques. Classic image processing methods typically adopt an approach that requires extracting meaningful features from raw data. In these methods, important features in the image are manually identified and extracted. In contrast, artificial intelligence-based methods automatically extract significant features from the image and learn directly. Additionally, these technological methods exhibit superior performance compared to traditional methods in terms of flexibility. Tech-

niques like deep learning and machine learning, within their subgroups, by leveraging pre-trained models, these techniques can uncover hidden relationships and underlying structures in the data. Furthermore, more accurate and reliable results can be achieved with large amounts of labeled data.

Traditional Methods

Active Contour Model

It is a curve model, initially defined on the image, utilizing visual cues like edges, intensity changes, and contrast. This model, known as the snake algorithm, actively moves to find object boundaries based on the principle of energy minimization and continually updates itself mathematically. It is commonly applied to grayscale images in edge detection and object segmentation tasks. ACM effectively follows real object boundaries by demonstrating high sensitivity in areas where pixel value changes are significant [8]. This feature offers an advantage in achieving highly effective results on structures with clear boundaries and high contrast. Additionally, it is recognized for providing excellent segmentation accuracy by dividing the image into segments and grouping pixels based on their similar features [9]. However, the method has some limitations. Generally, accurately segmenting multiple objects simultaneously can be challenging with classical active contour models. Furthermore, directing the contour in regions with low contrast or unclear edge information may be difficult, potentially negatively affecting the accuracy and stability of pixel grouping.

K-means Algorithm

K-means is an unsupervised clustering algorithm used to partition data into K distinct groups based on proximity to centroids. In traditional Active Contour Models, common problems such as under-segmentation and over-segmentation can occur, and in these cases, it is possible to process different types of images correctly by integrating the K-means algorithm into the energy function [10]. This algorithm offers various advantages when used in the fields of data analysis and machine learning. Notably, its high computational speed and efficiency, even with large datasets, make K-means attractive for practical applications. However, the most fundamental disadvantage of the algorithm is related to the number of clusters (K value) that must be determined in advance. If an inappropriate K value is selected, the clustering results obtained may lose their significance and cause the data structure to be incorrectly represented. In this context, the appropriate K value can be determined by calculating the inertia with the Elbow Method.

Grayscale images provide a representation based solely on light intensity, without color information. In such images, each pixel has a value between black and white, usually ranging from 0 to 255. Images that are noisy and contain low-quality weld errors converted to gray can be corrected using the active contour model, allowing for more accurate detection of object boundaries. Figure 1 shows images obtained using two different image processing algorithms on a grayscale image.

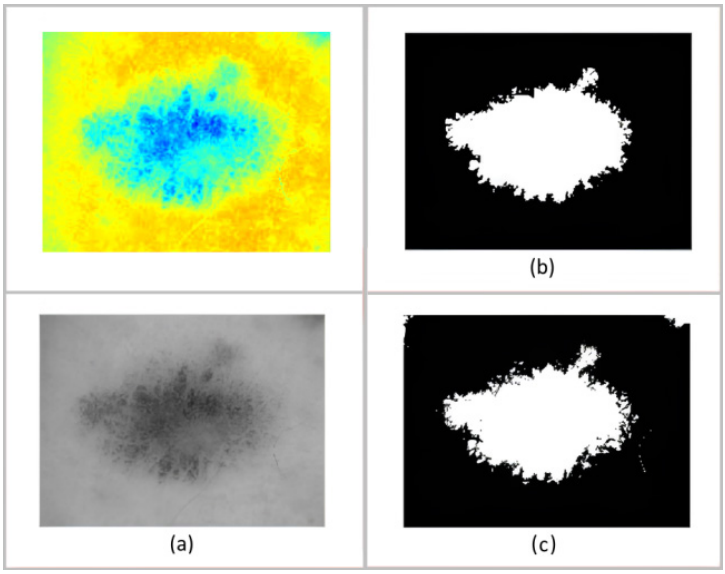

Figure 1. *Comparison of segmentation methods applied to a grayscale image: (a) original, (b) ACM, (c) K-means [11]*

Thresholding Algorithm

Thresholding is a basic image segmentation technique commonly used for foreground-background separation in grayscale and binary images. The decision is made by comparing the intensity of each pixel with a threshold value (T) determined between 0–255. If the pixel value is greater than T, it is accepted as white (object), and if not, it is assigned as black (ground). The thresholding algorithm may exhibit poor performance in complex and unevenly illuminated images due to its sensitivity to light changes [12]. In order to overcome this problem, local threshold values are determined for each pixel using adaptive thresholding methods. In this context, mean or weighted average (Gaussian) based approaches can be preferred. Adaptive thresholding techniques such as mean and Gaussian-weighted methods are commonly employed to address this issue.

However, since these approaches require separate calculations for each pixel, they increase the processing time and may decrease the overall speed of the algorithm. Table 1 provides a comparative analysis of three thresholding methods based on their key characteristics [13].

Table 1. *Feature-based comparison of classical image processing methods*

Feature	Thresholding	K-means	ACM (Active Contour)
Algorithm Speed	Very Fast	Medium	Slow
Light Sensitivity	High (Light Changes Affect)	More Robust	Robust Depending on Image Gradient
Complexity	Low (Works with Simple Logic)	Medium (Depending on Clusters)	High (Energy Function Includes Deformation)
Sensitivity	Low (Good for Simple Scenes)	Medium (Depending on Clusters)	High (Sensitive to Edges)
Information Requirement	Not Required (Uses Pixel Value Only)	Pixel Cluster's Location	Edge And Contour Information

Artificial Intelligence Based Methods

Convolutional Neural Networks (CNN)

Convolutional Neural Networks (CNNs) are a class of deep learning architectures widely used in image processing and visual recognition tasks. This method has been used as an effective tool in the detection of weld errors or types thanks to its ability to automatically extract important patterns and features on the image, and has played an important role in the detection of distinctive details such as shape, texture or distortions in weld images, especially in the feature recognition stage [14]. The Convolutional Layer, shown in Figure 2, forms the main building block of the algorithm and is responsible for detecting the features of the images. After this part is applied, more specific points of the images can be reached. The Activation layer allows the model to learn non-linear relationships, enabling more complex functions to be learned. The Rectifier (ReLU) function used in this context converts negative inputs to zero, allowing some neurons in the network to be disabled and thus allowing the model to work more efficiently with fewer active neurons. In addition, the ReLU function provides a faster calculation process compared to other activation functions by outputting zero when the input is less than zero and the input itself when it is greater than zero.

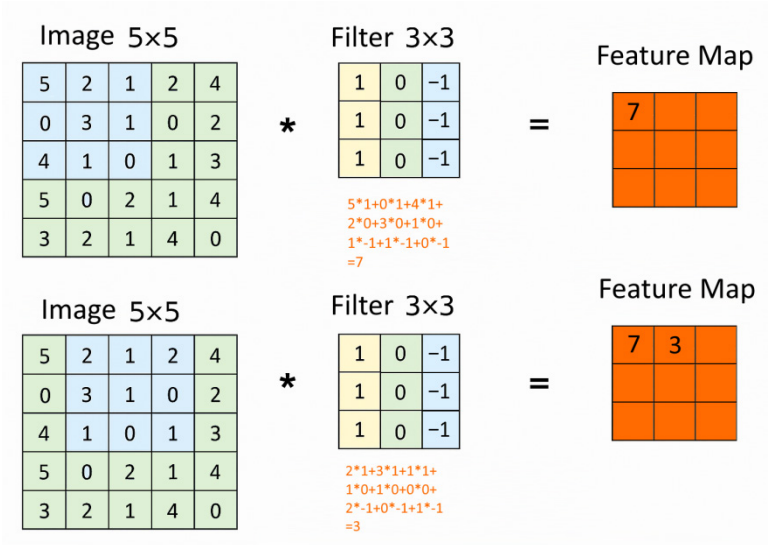

Figure 2. *Creation of a feature map from the input image in the convolutional layer [14]*

CNNs can work efficiently with fewer parameters, automatically extracting important features from images and ensuring accurate recognition of objects even when their positions change. In an image classification task, the first layers usually recognize edges or simple patterns, while deeper layers combine these basic features to learn more complex features of objects, thus creating more abstract and high-level representations. However, some deep learning models are considered "black boxes", which makes it difficult to understand how the models work and the reasons for their decisions. This can limit the reliability and interpretability of the model. In addition, it can be difficult to learn weights and obtain accurate results in some layers. This can lead to problems such as vanishing or exploding gradients. Furthermore, CNNs require substantial volumes of accurately labeled data to achieve high performance and generalize across diverse scenarios [15].

Transfer Learning

Transfer learning is a machine learning technique that allows a model trained on a task to be reused as a starting point in a different task, and can be effectively applied, especially in the field of image processing with CNN architectures [16]. It is analogous to leveraging prior experience to expedite learning in a related task. Transfer learning, especially in cases with limited data and computational resources, saves time and increases model performance by utilizing pre-trained models. In this respect, it is an

effective method frequently preferred in fields such as deep learning and image processing. However, in this method, performance may decrease in case of domain mismatch. If there are significant differences between the source task and the target task in terms of data distributions, feature spaces, or label structures, the model may make incorrect generalizations. This situation is called negative transfer and can seriously affect the performance of the model. In Table 2, pre-trained model architectures commonly used in the transfer learning method and other machine learning algorithms are presented in detail.

Table 2. *Comparative characteristics of three different model architectures*

Feature	ResNet	VGG	MobileNet
Release Year	2015	2014	2017
Architectural Structure	Residual blocks	3x3 convolution + 2x2 pooling	Depthwise separable convolution
Purpose	Avoiding gradient loss in deep networks	High accuracy with simple and homogeneous structure	Efficient performance on mobile devices
Number of Layers	Between 18–152	16 or 19	Relatively less
Calculation Cost	Medium–High	High	Low
Model Size	Medium	Large	Small
Performance (Accuracy)	High	High	Medium–High (efficiency focused)
Usage Area	Image classification, detection	Image classification	Real-time applications on mobile/embedded systems

YOLO (You Only Look Once)

YOLO (You Only Look Once) is a convolutional neural network architecture designed for real-time object detection. The most basic feature of this algorithm is that it detects all objects by processing them only once, unlike traditional methods that require multiple passes and a significant amount of CPU resources to analyze an image [17]. This feature provides a significant advantage, especially in terms of processing speed. In addition, by processing the image as a whole, this algorithm helps to better learn the relationships between the locations of objects and provides more accurate detections. Figure 3 illustrates the image labeling and model training workflow. This process continues with the examination of the accuracy and loss values of the model at the end of each epoch. According to this flow,

the generalization ability of the model can be increased with techniques such as rotation, reflection, scaling, and mix-up. In addition, choosing the appropriate model architecture is a factor that directly affects the performance of the model. At the end of the training process, the performance of the model can be evaluated, and metrics such as classification results and a number of parameters can be presented. During the training process, monitoring the accuracy and loss values of the model at the end of each epoch is important to evaluate the effectiveness of the model's learning process.

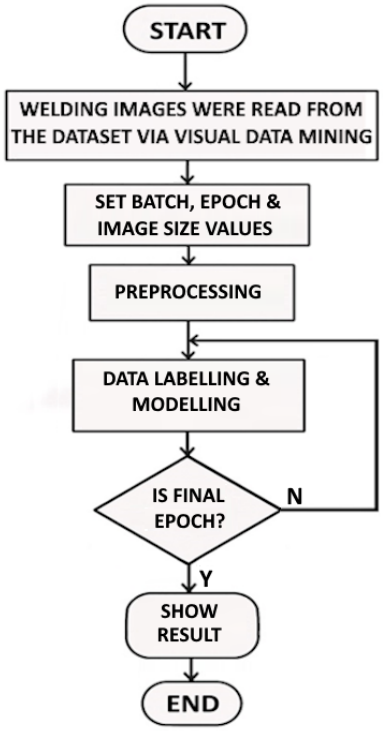

Figure 3. *Workflow of YOLO-based image processing and training pipeline*

The selection of the appropriate model architecture for this deep learning-based algorithm is of critical importance, especially in terms of compatibility with the task definition and dataset. Careful monitoring of the training process and the application of appropriate optimization techniques play a decisive role in increasing the overall performance of the model. Thus, not only is an increase in processing speed achieved, but also high performance can be achieved using low computational resources. Epoch and batch size are key hyperparameters that directly influence training efficiency and learning outcomes. These two concepts directly affect the efficiency and success of the learning process by determining how and how often the model is fed with data.

The integration of the YOLO algorithm with various simulation software significantly increases the environmental perception and decision-making capabilities of robotic systems, allowing more flexible and autonomous operations in applications such as production, assembly, and quality control. Thanks to this integration, robots can recognize objects in their environment in real time and plan their movements based on this information. Accordingly, the visual perception and response capabilities of robots can be evaluated with deep learning methods in the simulation environment of RoboDK. Thus, possible problems that may be encountered in real-world applications can be detected in advance, and the accuracy and reliability of software studies can be increased. In addition, error reduction can be achieved with a deep learning-based approach by taking multiple images while gradually advancing towards the target center using the correspondence relationship between world coordinates and image coordinates [18]. In addition to these fast detection algorithms based on deep learning, fuzzy logic-based segmentation methods also have an important place in image analysis.

Fuzzy C-Means (FCM) Algorithm

Fuzzy C-Means (FCM) is a soft clustering algorithm that extends K-means by incorporating fuzzy logic to handle uncertainty in image segmentation tasks [19]. This algorithm works by assigning the membership degree to the relevant clusters to each data instead of dividing the data into sharp classes. This approach provides more accurate results in data with uncertain or fuzzy boundaries. Each data point is represented by the membership degrees of the clusters, creating a flexible structure. In this way, a more precise and accurate clustering is performed by considering the possibility of data points belonging to more than one cluster. In Figure 4, more detailed segmentation was performed with the FCM algorithm after the weld pool preprocessing. Accordingly, a structure with more than one closed contour is observed at the outer boundary of the weld pool, while the noise effect is especially evident in the region close to the tail, and the outer line merges on both sides [20]. The FCM model developed for this problem pre-segments the weld pool image and defines a starting contour close to the weld pool contour, thus providing an effective solution.

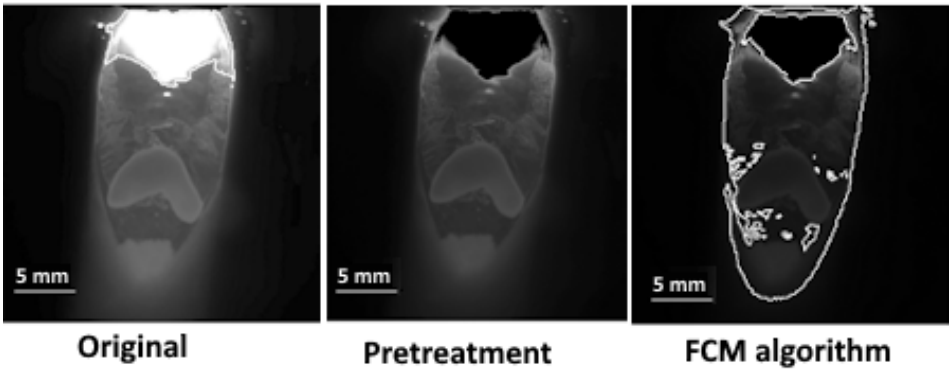

Figure 4. *Segmentation Enhancement of a Weld Pool Image Using the FCM Algorithm [20]*

The FCM algorithm improves weld pool segmentation by defining an initial contour that closely aligns with the actual boundary. Segmentation-based methods offer significant advantages over classical approaches in terms of flexibility, accuracy, and automation potential.

Simulation Programs and Software

RoboDK is a comprehensive software platform developed for offline programming and simulation of industrial robots, especially for industrial welding stations [21]. Thanks to its support for hundreds of different robot brands, it can work with a wide range of hardware. Thanks to its offline programming capabilities, the control codes of robotic systems can be tested and optimized in a simulation environment and then transferred directly to real robots. SolidWorks can be integrated with OpenCV-based tools, facilitating the transfer of design data into robotic systems. This simulation program allows users to develop customized scenarios and dynamically control robot movements with API support accessible via the Python programming language. Thanks to all these features, RoboDK is used as an effective tool not only for motion simulation but also for the development of camera integration and image processing-based robot applications. Figure 5 displays the RoboDK interface, where Section A contains Python code implementations, and Section B shows the configuration panel for adjusting camera resolution.

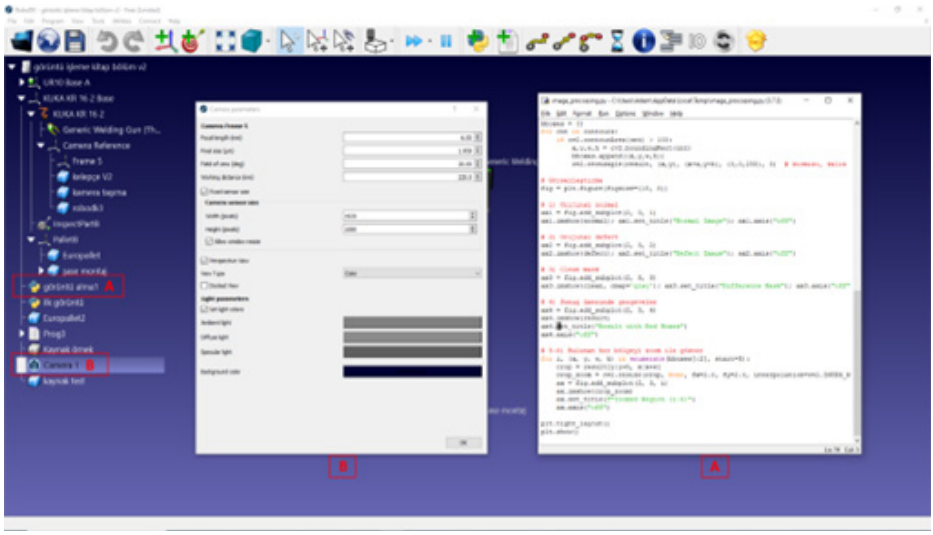

Figure 5. *Camera Settings and Programming Interfaces in RoboDK*

A welded test sample measuring 483 mm in length was designed in SolidWorks and exported in STEP214 format. In order to examine this sample, a camera piece with dimensions of 70x30x25 mm was created, and it was also converted to STEP214 format. Thus, these parts converted to the appropriate format could be imported to the RoboDK program. While preparing the weld sample piece, defects such as thickness differences, cracks and holes were created. The performs the simulation prepared to examine one of these defects, a 6-axis Kuka KR 16-2 robot with a length of 1611 mm was imported from the library. In this simulation, the camera resolution setting was set to 640x480 pixels; in the optical settings, the focal length was 6 mm, the field of view was 32 degrees, and the farthest clear viewing distance was preferred as 300 mm. As a result of these adjustments, the position of the camera was determined appropriately and fixed to the last axis of the robot. In this way, the error image was obtained through the system moving synchronously with the robot, and the defective weld image presented in Figure 6 was recorded and stored for use in subsequent analysis.

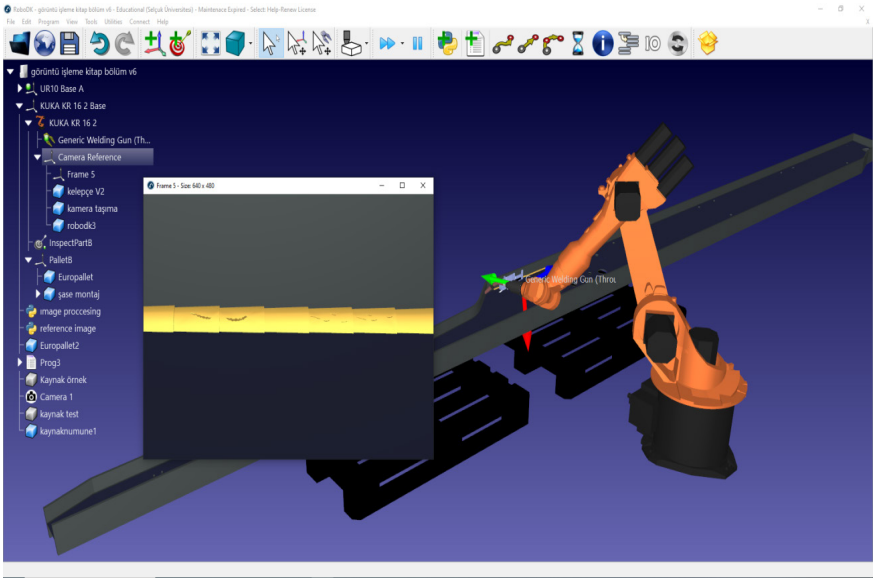

Figure 6. *Obtaining the defective weld image in the RoboDK*

Active Contour Model (ACM) was preferred in the first simulation study because it is an effective method for extracting differences by masking in the field of image processing. In this model, a contour line is usually defined as a rectangle at the beginning of the process, and this contour progresses by evolving towards the object edges in the image. The movement of the contour is directed in a way that minimizes the energy. While the internal energy here ensures that the contour remains smooth and continuous, the external energy directs the contour towards the object boundaries with the edge information in the image. At the end of the process, the contour fits around the target object, and thus the segmentation process is performed. The output of ACM is usually a binary mask, and the object interior regions are represented as white (1) and the exterior regions as black (0). In this context, the difference mask extraction result obtained is presented in Figure 7.

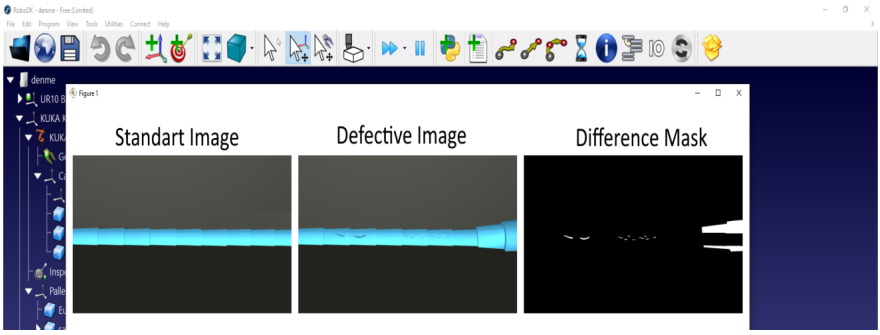

Figure 7. *Difference mask obtained from the two different images using the ACM method*

The Active Contour Model (ACM) used in the RoboDK simulation program differs significantly from traditional gray-level difference methods in terms of its basic approach. Gray level difference methods aim to detect pixel-level intensity differences between two different images, and the output of these methods is usually in the form of a grayscale difference map and is pixel-based. The image processing-based method preferred to overcome these shortcomings focuses on precisely detecting the boundaries of specific objects in the image; the output obtained as a result of this process is in a binary mask format that carries the segmentation information related to the object. In this context, ACM is sensitive not only to pixel differences but also to the structural properties of object edges, and in this respect provides higher-level semantic information.

The second simulation study aimed to improve the generalization ability of the YOLO-based model and to obtain a more robust and error-tolerant system. Various data augmentation techniques have been applied to achieve these goals. In this context, mixup, rotation, and reflection techniques have been applied to increase the variety and number of training data. To facilitate more accurate object detection in the deep learning model, a dataset consisting of 285 images, including defective images and images of flawless metal parts, has been used for the Yolov5 algorithm, and it is thought that hypothesized that classification accuracy can be improved by using a dataset containing more images [22]. Based on the insufficient number of visual data used in the study in the literature, 520 images have been prepared for use in deep learning in this study. Some of these images, created thanks to data augmentation techniques, are presented in Figure 8.

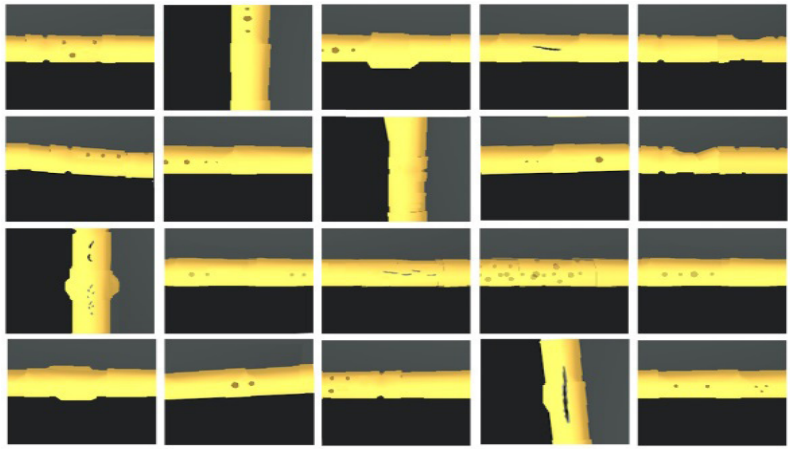

Figure 8. *Some images used in the training of the YOLO algorithm*

The YOLO algorithm performs the classification of weld images and the estimation of their bounding boxes with a single neural network. In this process, it uses frames of $S \times S$ dimensions and estimates parameters such as the center coordinates of the boxes (x, y), width (w), height (h), and assigns a confidence score between 0 and 1 for each predicted object [23]. The bounding box used in this section is a rectangular frame used to indicate the location of some defects in the image in weld defect detection tasks [24]. A visual test dataset with a resolution of 640x480 pixels was analyzed 25 times. In the test data shown in Figure 9, large cracks were successfully classified as 'Class 0' and small cracks as 'Class 1'.

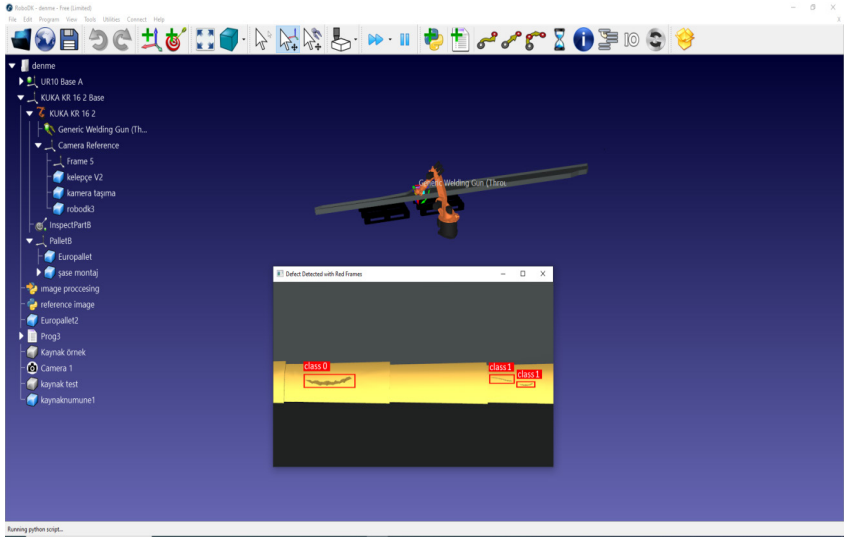

Figure 9. *Defective weld location and its class using the Yolov5*

Conclusion

This study presented a comparative evaluation of the ACM and the YOLO algorithm in the context of detecting welding defects within a simulated dataset generated in the RoboDK environment. While both methods were effective in identifying weld anomalies, they exhibited distinct differences in terms of detection accuracy, computational efficiency, and suitability for real-time industrial applications.

The ACM approach yielded effective results, particularly in accurately delineating edge boundaries and identifying shape-based anomalies. Nonetheless, its relatively low processing speed and the necessity for manual parameter tuning limit its suitability for real-time applications within simulation environments. In contrast, the YOLOv5 algorithm, which incorporates automatic parameter optimization and leverages data augmentation techniques, has emerged as a more favorable alternative for simulation studies. The incorporation of data augmentation significantly enhanced the model's generalization capability by increasing the diversity of training images. Using the YOLOv5-small model, an F1 score of 0.74 was achieved, supported with an average confidence level of 0.39. Moreover, a robust validation protocol—conducted across 25 training iterations—enabled the successful detection of overfitting and underfitting scenarios. In a subsequent experiment involving the YOLOv5-large model, which entailed an increased number of layers, parameters, and computational capacity, the training process was extended to 50 epochs. This refinement led to an improved F1 score of 0.79, and a confidence score of 0.53, indicating a substantial enhancement in classification performance.

Evaluation results suggest that while ACM offers advantages in processing speed and high boundary sensitivity, its reliance on an initial contour renders it inadequate for detecting multiple objects within a frame. Conversely, the YOLO algorithm, trained on a substantially larger dataset, demonstrated superior performance in multi-object detection tasks.

Furthermore, the findings highlight the potential of integrating deep learning algorithms, such as YOLO, with simulation platforms like RoboDK to enhance robotic systems' environmental awareness and responsiveness. This integration could significantly improve the effectiveness of robotic applications in both simulated and real-world environments. It is also suggested that ACM's precision in edge detection may complement YOLO's robust object detection capabilities. Therefore, a hybrid framework combining both methodologies may provide a more comprehensive and powerful solution for automated defect detection in future research.

References

1. Martinez, R. T., & Alfaro, S. C. A. (2020). Data analysis and modeling techniques of welding processes: The state-of-the-art. In Welding-Modern Topics. IntechOpen.
2. Melnikov, P., Bobrov, A., & Marfin, Y. (2022). On the use of polymer-based composites for the creation of optical sensors: a review. Polymers, 14(20), 4448.
3. Rosca, C. M. (2023). Comparative Analysis of Object Classification Algorithms: Traditional Image Processing Versus Artificial Intelligence—Based Approach. *Rom. J. Pet. Gas Technol*, 169-180.
4. Roca Barceló, F., Jaén del Hierro, P., Ribes Llario, F., & Real Herráiz, J. (2018). Development of an ultrasonic weld inspection system based on image processing and neural networks. *Nondestructive Testing and Evaluation*, *33*(2), 229-236.
5. Zhang, Wenying, Min Dong, and Li Jiang. "Image segmentation using convolutional neural networks in multi-sensor information fusion." *Soft Computing* 27.23 (2023): 18353-18372.
6. Lang, X., Ren, Z., Wan, D., Zhang, Y., & Shu, S. (2022). MR-YOLO: An improved YOLOv5 network for detecting magnetic ring surface defects. *Sensors*, *22*(24), 9897.
7. Sarivan, Ioan-Matei, Ole Madsen, and Brian Vejrum Wæhrens. "Automatic welding-robot programming based on product-process-resource models." *The International Journal of Advanced Manufacturing Technology* 132.3 (2024): 1931-1950.
8. Abdelsamea, Mohammed M., Giorgio Gnecco, and Mohamed Medhat Gaber. "An efficient Self-Organizing Active Contour model for image segmentation." *Neurocomputing* 149 (2015): 820-835.
9. Chen, Bo, et al. "A fractional order derivative based active contour model for inhomogeneous image segmentation." *Applied Mathematical Modelling* 65 (2019): 120-136.
10. Ge, P., Chen, Y., Wang, G., Weng, G., & Chen, H. (2023, May). An active contour model driven by K-means clustering for image segmentation. In *2023 35th Chinese* Control and Decision Conference (CCDC) (pp. 4595-4600). IEEE.
11. Göreke, V. (2025), Medikal görüntü segmentasyonu: geleneksel yöntemler ve kod uygulamaları, *Bilgisayar Bilimleri ve Mühendisliği Alanında Araştırmalar ve Değerlendirmeler - Mart 2025* (ss. 23–47). Gecekitaplığı Kitabevi.
12. Seelaboyina, Radha, and Rajeev Vishwakarma. "Different thresholding techniques in image processing: A review." *ICDSMLA 2021: Proceedings of the 3rd International Conference on Data Science, Machine Learning and Applications*. Singapore: Springer Nature Singapore, 2023.

13. Liu, T., Zheng, P., & Bao, J. (2023). Deep learning-based welding image recognition: A comprehensive review. *Journal of Manufacturing Systems*, *68*, 601-625.

14. Wang, Zhenzhou. "Robust thresholding by calibration." *IECON 2017-43rd Annual Conference of the IEEE Industrial Electronics Society*. IEEE, 2017.

15. Sultana, Tasleem, and Motahar Reza. "Identification of Potato Leaf Diseases Using Hybrid Convolution Neural Network with Support Vector Machine." *International Advanced Computing Conference*. Cham: Springer Nature Switzerland, 2022.

16. Gupta, Jaya, Sunil Pathak, and Gireesh Kumar. "Deep learning (CNN) and transfer learning: a review." *Journal of Physics: Conference Series*. Vol. 2273. No. 1. IOP Publishing, 2022.

17. Pande, Sagar Dhanraj, and Raghav Agarwal. "Multi-class kidney abnormalities detecting novel system through computed tomography." *IEEE Access* 12 (2024): 21147-21155

18. Anjum, Muhammad Umar, et al. "Vision-based hybrid detection for pick and place application in robotic manipulators." *2023 International Conference on Robotics and Automation in Industry (ICRAI)*. IEEE, 2023.

19. Jiao, Z., Qin, H., Gao, X., Feng, Z., Xu, Y., Chen, S., ... & Liu, W. (2023). Image processing and feature extraction for hull structure GMAW based on weld pool visual sensing. *Journal of Sensors*, *2023*(1), 6317992.

20. Fang, J., & Wang, K. (2019). Weld pool image segmentation of hump formation based on fuzzy C-means and Chan-Vese model. *Journal of Materials Engineering and Performance*, *28*, 4467-4476.

21. Pollák, Martin, and Karol Goryl. "Simulation Design and Measurement of Welding Robot Repeatability Utilizing the Contact Measurement Method." *Machines* 11.7 (2023): 734.

22. Özyer, B., & Taspinar, Y. S. (2024). Realising Quality Control of Metal Products Used in Industry Through Deep Learning. *Intelligent Methods In Engineering Sciences*, *3*(4), 118-125.

23. Singh, A., Kalaichelvi, V., DSouza, A., & Karthikeyan, R. (2022). GAN-Based image dehazing for intelligent weld shape classification and tracing using deep learning. *Applied Sciences*, *12*(14), 6860.

24. Babu, K. Mahesh, and M. V. Raghunadh. "Vehicle number plate detection and recognition using bounding box method." 2016 International Conference on Advanced Communication Control and Computing Technologies (ICACCCT). IEEE, 2016.

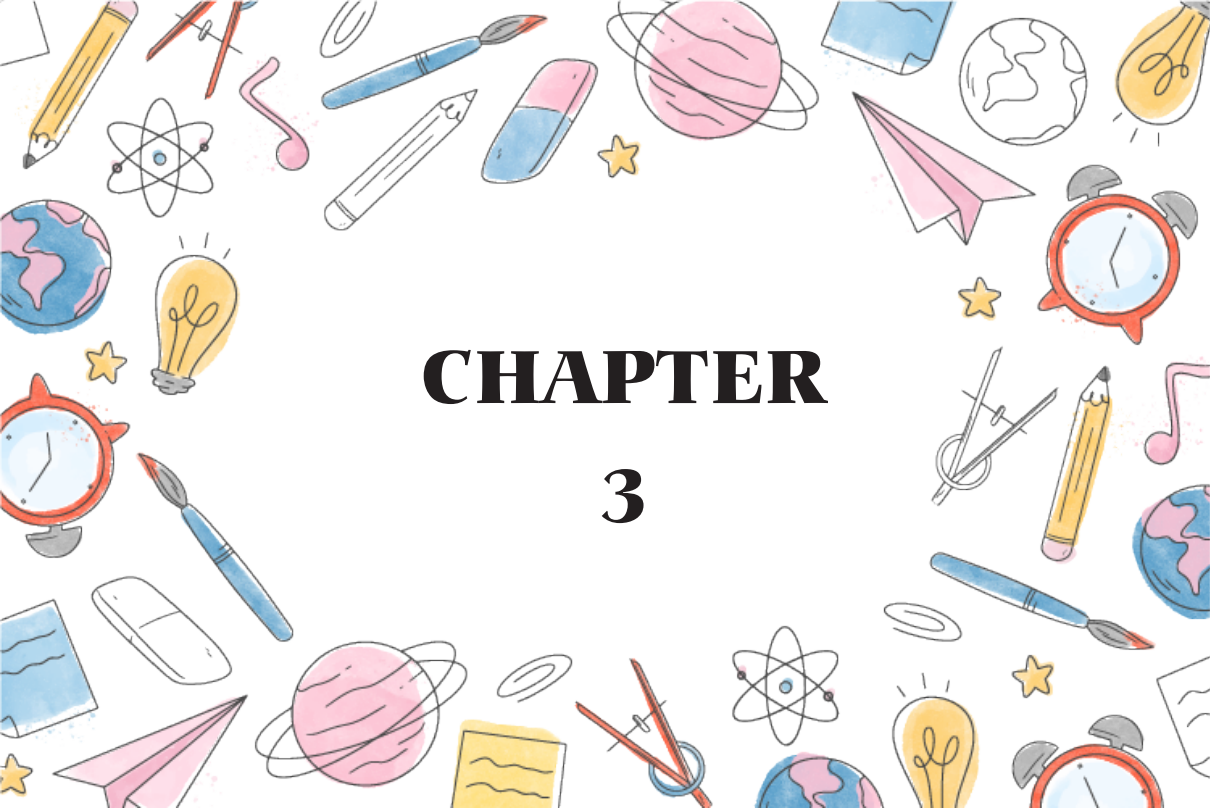

CHAPTER 3

BACTERIOLOGICAL AND PHYSICOCHEMICAL EVALUATION OF WATER QUALITY AT SOME POINTS ON THE KARASU RIVER, ERZINCAN, TURKEY

Fatih YILMAZ [1]

Gokhan Onder ERGUVEN [2]

Numan YILDIRIM [3]

1 Erzincan Environment, Urbanization and Climate Change Directorate, Branch Directorate Responsible for EIA and Environmental Permits, Erzincan, Turkiye, k.fatihyilmaz@hotmail.com, ORCID: 0009-0002-9279-6378

2 Assoc. Prof. Dr., Munzur Unıversity, Faculty Of Economics And Administrative Sciences, Department Of Politıcal Science And Public Administration, Department Of Urbanıization And Environmental Issues, Tunceli, Turkiye, gokhanondererguven@gmail.com, ORCID: 0000-0003-1573-080X

3 Prof.Dr., Munzur University, Tunceli Vocational School, Department, of Plant and Animal Production, Organic Agriculture Programme, Tunceli, Turkiye, numanyildirim44@gmail.com, ORCID: 0000-0003-1109- 8106

INTRODUCTION

Water is one of the most essential resources for the existence and continuity of life. It is an indispensable compound that sustains life, from the smallest microorganisms to the largest living organisms. Water plays a vital and irreplaceable role in numerous physiological functions, including the absorption and transport of nutrients to cells, the proper functioning of digestive processes, the maintenance of homeostatic balance in the functions of cells, tissues, and organs, the removal of harmful waste products from the body, and the regulation of body temperature (URL-1, 2024).

Although water covers approximately 70% of the Earth's surface, only about 2.5% of this is freshwater, and a mere 10% of that freshwater is available for use. Accessible clean water resources are derived from surface waters such as lakes, reservoirs, rivers, and streams. This amount constitutes approximately 0.10% of the total freshwater potential on Earth. The remaining volume primarily consists of saline water, which is not directly suitable for drinking purposes (URL-2, 2024).

River ecosystems are vital resources for both aquatic wildlife and human needs, and any changes in their environmental quality or water renewal rates can have far-reaching ecological and societal consequences (Vincent, 2009). One commonly discussed category of pollutants is domestic waste. Approximately 20–30% of human waste consists of undigested food, while the remainder comprises bacteria and wastewater (Ormerod et al., 1982).

The Upper Euphrates Basin, located within the Eastern Anatolia Region, is a significant receiving body and irrigation source that supports both population and industrial activities. In this region, agricultural irrigation is regularly carried out in all seasons, while wastewater discharges from surrounding industrial sectors and settlements may also reach water bodies. Physicochemical and bacteriological analyses will be conducted on samples collected during the spring and autumn seasons at stations to be identified in the area. The results will be evaluated and compared with the national Surface Water Quality Regulation to assess the pollution load resulting from industrialization and urbanization.

WATER POLLUTION

Water pollution can affect various water sources, including surface waters (rivers, lakes, seas) and groundwater, significantly reducing their suitability for purposes such as drinking, agricultural irrigation, and industrial use. Common sources of pollution include industrial discharges, chemical fertilizers and pesticides from agricultural activities, domestic wastewater, stormwater runoff, and natural events such as volcanic eruptions

and landslides (Yılmaz et al., 2020). These pollutants alter the physical, chemical, and biological properties of water, thereby negatively impacting its quality. Water pollution poses serious threats to both ecosystem and human health; it can result in the death of aquatic organisms, contamination of agricultural produce, and an increased risk of waterborne diseases (Bulut et al., 2012).

Water quality refers to the assessment of the chemical, physical, and biological characteristics of water and determines its suitability for specific uses (Bilgin, 2015). A variety of parameters are employed to evaluate water quality, broadly classified into physicochemical and biological indicators (Srivastava et al., 2017). Physicochemical parameters include measurements of water's physical and chemical properties such as dissolved oxygen (DO), pH, temperature, salinity, conductivity, and total dissolved solids (TDS).

Biological parameters, on the other hand, are used to assess the microbiological quality of water (Kalyoncu & Serbetci, 2013). Among these, coliform bacteria—especially Escherichia coli (E. coli)—are widely used as biological indicators in water quality assessments. Coliforms are indicative of fecal contamination from human or animal waste, and their presence in water samples signals the existence of fecal pollution (Hosmani, 2012).

Types of water pollution are generally classified based on the sources of pollutants and their impacts on water. Point-source pollution refers to contamination originating from a single, identifiable source (Baştürk, 2019), such as industrial facilities that discharge wastewater directly into water bodies. These pollutants, often including chemicals from factory outlets, can severely disrupt the physicochemical balance of aquatic environments (Aras et al., 2017). In contrast, non-point source pollution is more difficult to control, as contaminants are dispersed over large areas and stem from multiple sources, making identification and management more complex (Köse et al., 2020).

Coliform bacteria, including E. coli and other fecal microorganisms, are responsible for the transmission of waterborne diseases (Tezcanli Guyer & İlhan, 2011).

One of the key indicators for assessing water quality in river ecosystems is microbiological analysis. Coliform bacteria are among the most widely used parameters for detecting microbial contamination in river water. They provide critical information on fecal pollution and are essential indicators of hygienic water quality (Ács et al., 2005). Discovered in 1885 by Theodor Escherich, Escherichia coli is particularly prevalent in environments contaminated with human feces and is commonly used to assess water pollution levels. Considering that even a single gram of human waste

can contain a high concentration of these bacteria, monitoring the density of coliforms in water sources is crucial for protecting public health (Guo-chen et al., 2012).

Monitoring water quality in areas such as the Karasu River—where intensive agricultural and industrial activities take place—is not only essential for preserving environmental health but also critical for ensuring the sustainability of economic activities.

KARASU RIVER

Fırat Nehri, Karasu ve Murat kollarının birleşmesiyle oluşmaktadır. Karasu Nehri, uzunluk açısından en büyük kol olmamasına rağmen, tarih boyunca Fırat olarak anılmış ve nehrin ana kolu olarak kabul edilmiştir. Bu nedenle, Karasu'nun kaynağı olan ve Erzurum Ovası'nın kuzeyindeki Dumlu Dağı'ndan çıkan Dumlu Suyu, Fırat Nehri'nin başlangıç kolu sayılmaktadır. Karasu Nehri, Erzurum Ovası'ndan geçtikten sonra, Aşkale'den itibaren batısında bulunan derin ve dar vadilere yönelir. Aşkale ile Tercan arasındaki kesimde keskin dönüşler yaparak önce güneye, sonra batıya doğru ilerler. Bu süreçte sol tarafından Tuzla Suyu'nu alarak Sansa Boğazı adlı dar ve derin bir geçide girer. Boğazdan çıktıktan sonra, yatak değişiklikleri yaparak Erzincan Ovası'ndan geçer. Erzincan Ovası'nın batısında, Kemah ile ova arasında yer alan Kemah Boğazı'na ve Kemah ile İliç ilçeleri arasındaki Atma Boğazı'na giren nehir, bu iki boğazda yüzlerce metre yüksekliğinde, dik kayalıklarla çevrili dar alanlardan akmaktadır. İliç'in batısında ani bir dönüşle güneye yönelen Karasu Nehri, bu noktada Divriği'den gelen Çaltı Suyu ile birleşir. Nehir, kenarları oldukça dik ve dar olan Sandık Boğazı'ndan geçerek Kemaliye yönüne ilerler. Daha güneyde, sağ taraftan Arapkir Suyu'nu aldıktan sonra, Keban ilçesinin yaklaşık 10-12 km kuzeyinde Murat Nehri ile birleşerek Fırat Nehri'ni oluşturur. Karasu ve Murat kollarının birleşme noktası günümüzde Keban Baraj Gölü suları altında kalmıştır. Karasu Nehri'nin Keban Barajı'na kadar olan uzunluğu 460 kilometredir (Tuncel M, 2024).

The Karasu River plays a vital role in agricultural irrigation in the region, and its water quality directly affects both crop productivity and human health. Contamination of river water may lead to the accumulation of toxic substances in plants grown in the area, resulting in long-term environmental and societal damage (Shen et al., 2018). Therefore, periodic monitoring of water quality and timely implementation of appropriate measures based on the findings are essential for achieving sustainable development goals in the region (Hwang et al., 2006).

The Karasu River holds strategic importance in terms of irrigation and energy-related activities. Due to its direct exposure to the surrounding

environment, river ecosystems are particularly vulnerable to both natural processes and anthropogenic activities (Srivastava et al., 2017). The sustainability of aquatic ecosystems is vital for the survival of animal and plant species inhabiting these environments. Deterioration in water quality may threaten biodiversity, leading to species extinction or migration from their habitats (Hosmani, 2012). Moreover, the suitability of river water for human use varies depending on the level of pollution and may pose significant health risks.

In the region, agricultural activities heavily depend on the use of river water for irrigation, while industrial facilities utilize the Ergene River both as a water source and a discharge point for wastewater. This dual use significantly disrupts the river's natural hydrological cycle and adversely affects water quality (Venkatachalapathy & Karthikeyan, 2015). Industrial and domestic discharges into the river gradually impair both the chemical and biological balance of the water, resulting in increased pollution and serious ecological problems (Noga, Stanek-Tarkowska, Kochman et al., 2013).

POLLUTION SOURCES AND IMPACTS OF KARASU RIVER

The Karasu River, one of the two main tributaries of the Euphrates, originates in the province of Erzurum and passes through numerous settlements, during which it incorporates a wide range of physical, chemical, and biological pollutants. As the river flows downstream, it not only transports these pollutants to many other residential areas but also contributes to their dilution, while simultaneously creating significant challenges for the remediation of existing pollution. Two primary sources of pollution affecting the Karasu River are domestic wastewater and agricultural activities.

Impact of Domestic Wastewater

Pollutants originating from domestic wastewater enter surface waters through various pathways, contributing significantly to water pollution (Ram et al., 1990). In particular, sewage and detergents are among the main contributors to elevated chemical oxygen demand (COD) levels, which negatively affect biological processes in aquatic environments and jeopardize the sustainability of aquatic life.

Domestic wastewater contains coliform bacteria and especially Escherichia coli (E. coli), which are key microbial pollutants. These pathogens cause serious microbiological contamination, rendering water unsafe for human consumption, particularly when inadequately treated sewage is discharged directly into the river (Oskay et al., 2023). The presence of these pathogens increases the risk of waterborne diseases such as diarrhea, typ-

hoid, and dysentery, especially in areas close to human settlements, thereby posing a direct public health risk and increasing healthcare expenditures (Xue et al., 2023).

In smaller settlements, infrastructure deficiencies result in wastewater from residences that are not connected to sewer systems being discharged into the river via septic tanks or open channels (Noga, Stanek-Tarkowska, Pajączek et al., 2013). This not only increases the pathogenic load but also causes fluctuations in organic matter, nitrogen, and phosphorus concentrations. The elevated nutrient levels promote eutrophication, leading to algal blooms, oxygen depletion in the water column, and mass fish mortality (Szczepocka et al., 2014).

The use of untreated or partially treated wastewater for irrigation purposes has been shown to cause soil salinization (Ubay et al., 1995; Stewart & Flinn, 1984) and the accumulation of toxic substances (Bouwer & Chaney, 1974). Moreover, the reuse of sewage water in agriculture results in an increase in soil pH levels (Ergene, 1993), which adversely affects soil structure and crop productivity.

Addressing domestic wastewater-induced pollution requires the implementation of advanced treatment technologies, the modernization of insufficient treatment facilities, and the improvement of local water management policies. Furthermore, raising public awareness and encouraging individual water-saving behaviors can significantly contribute to reducing the environmental damage caused by domestic discharges (Tokatlı et al., 2020).

Impact of Agricultural Activities

Pollutants originating from agricultural activities not only deteriorate the chemical composition of water but also alter its physical characteristics. Sediments and soil particles carried into the river as a result of erosion from agricultural lands increase turbidity and reduce light penetration (Çelekli et al., 2024), thus impairing photosynthesis in aquatic plants and disrupting the energy flow within the ecosystem.

During agricultural irrigation, part of the water is lost through evaporation, while the remaining water carries organic matter into the river via erosion. The accumulation of organic matter lowers dissolved oxygen levels and increases biological oxygen demand (BOD), leading to hypoxic conditions and mortality among aquatic organisms (Xue et al., 2023).

Nitrogenous compounds such as nitrate, nitrite, and ammonium nitrogen present in wastewater significantly contribute to environmental pollution (Bauchard et al., 1992). In addition to organic matter, domestic was-

tewater also contains considerable levels of nutrients such as nitrogen and phosphorus (Atabay et al., 1995).

The widespread agricultural lands within the Karasu basin facilitate the transport of fertilizers and pesticides into the river. Nitrogen- and phosphorus-based fertilizers are particularly prone to being washed into the river through surface runoff during rainy periods, while organophosphate and organochlorine pesticides pose acute toxicity risks to aquatic life. Moreover, tillage-induced erosion increases suspended particulate loads, further reducing light penetration and inhibiting the growth of photosynthetic aquatic vegetation (Szczepocka et al., 2014).

The cumulative effects of agricultural activities on the Karasu River present not only a threat to environmental sustainability but also a significant risk to public health in the region (Cankaya et al., 2023).

MATERIAL AND METHOD

In this study, water samples were collected during the spring and autumn seasons of 2024 from five designated stations along the Karasu River (before Vasgird Stream, after Vasgird Stream, the agricultural field region, before the wastewater treatment plant discharge channel, and after the wastewater treatment plant discharge channel). In situ measurements of physicochemical parameters such as dissolved oxygen (DO), temperature, pH, salinity, conductivity, and total dissolved solids were carried out simultaneously at the sampling sites using a multiparameter probe (Multi 340i/SET WTW) or an equivalent device.

Bacteriological analyses were conducted in the laboratory after transporting the samples in ice-cooled containers. For this purpose, the Multiple Tube Fermentation Technique (SM 9221B) (APHA, 2005) was employed to identify coliform bacteria. This fermentation method is a three-step procedure consisting of the presumptive, confirmed, and completed tests. The results are statistically expressed as the Most Probable Number (MPN). A five-tube test format was used to ensure analytical accuracy.

For the analysis of Chemical Oxygen Demand (COD), the open reflux method described in Standard Method 5220B was utilized. For biochemical analyses, five-day Biochemical Oxygen Demand (BOD_5) tests using Oxitop instruments or the Winkler method were employed (Figure 1).

Figure 1. *Sampling points*

The five designated sampling points along the Karasu River are illustrated in Figure 1. Additionally, the coordinates and selection rationale for each sampling location are as follows:

The Vasgird Stream flows from north to south through the city and is situated on the relatively western side of the urban area. Due to the presence of unauthorized discharge points as it passes through the city, the pollution contribution of this stream was taken into consideration during site selection.

Photograph 1 shows the sample collection during the spring season from the pre-confluence point of Vasgird Stream (39°42’0.99”N, 39°28’4.34”E), while Photograph 2 depicts the sample collection from the same point during the autumn season.

Photograph 1. *Vasgird Stream Before Confluence – Spring Sampling*

Photograph 2. *Vasgird Stream Before Confluence – Autumn Season*

Photograph 3 shows the sample collection during the spring season from the post-confluence point of Vasgird Stream (39°41’52.41”N, 39°27’45.11”E), while Photograph 4 depicts the sample collection from the same location during the autumn season.

Photograph 3. *Post-Confluence Point of Vasgird Stream – Spring Season*

Photograph 4. *Post-Confluence Point of Vasgird Stream – Autumn Season*

Due to intensive agricultural activities along the banks of the Karasu River, the agricultural field area was selected as another sampling site. Photograph 5 shows the sample collection during the spring season at the Field Area point (39°42’7.44”N, 39°27’4.42”E), while Photograph 6 depicts the sample collection at the same location during the autumn season.

Photograph 5. *Tarla Region Spring*

Photograph 6. *Tarla Region Autumn*

The Wastewater Treatment Plant (WWTP) operated by the Erzincan Municipality discharges into the water channel that flows into the Karasu River. The pollution load from this facility to the river is one of the primary reasons for selecting this sampling point. Photograph 7 shows the sample collection during the spring season at the pre-confluence point of the WWTP discharge channel (39°41'42.53"N, 39°25'38.19"E), while Pho-

tograph 8 depicts the sample collection at the same location during the autumn season.

Photograph 7. *Spring Sampling at the Pre-Confluence Point of the WWTP Discharge Channel*

Photograph 8. *Autumn Sampling at the Pre-Confluence Point of the WWTP Discharge Channel*

Photograph 9 shows the sample collection during the spring season from the post-confluence point of the WWTP discharge channel (39°41’41.20”N, 39°25’24.76”E), while Photograph 10 depicts the sample collection from the same location during the autumn season.

Photograph 9. *Spring Sampling at the Post-Confluence Point of the WWTP Discharge Channel*

Photograph 10. *Autumn Sampling at the Post-Confluence Point of the WWTP Discharge Channel*

Dissolved Oxygen

Measurements were conducted instantaneously according to the TS 5677 EN 25814 standard. The membrane electrode method is a practical and preferred technique in the field due to its rapid results and the advantage of not requiring chemicals or glassware. Therefore, this method was chosen for on-site measurements.

Conductivity

Measurements were performed in situ instantaneously according to the TS 9748 EN 27888 standard. Conductivity is a quantitative indicator of the ability of an aqueous solution to conduct electric current. Therefore, it was included among the parameters to be examined in the Karasu River.

pH

The device used for pH measurements was calibrated and employed on-site. Measurements were conducted according to the TS EN ISO 10523 standard.

Temperature

Temperature values were recorded by reading a thermometer according to the SM 2550 B method.

Total Dissolved Solids (TDS)

Since the Multi 340i/SET WTW device used for measurements did not include a TDS measurement function, the TDS parameter was estimated through conversion from conductivity. Because the conductivity of the water in the Karasu River is below 1000 μS/cm, a conversion coefficient of 0.68 was applied.

Salinity

Salinity was determined using the SM 2520 B method.

Biochemical Oxygen Demand (BOD)

BOD analyses were conducted according to the SM 5210 B method. The decrease in dissolved oxygen observed in the BOD bottle directly correlates with the amount of biodegradable organic matter. In samples naturally containing microorganisms, such as domestic wastewater, external microbial inoculation is not necessary. The standard BOD test is performed at 20 °C in the dark with an incubation period of five days (URL-3, 2025).

Chemical Oxygen Demand (COD)

COD determination in wastewater samples includes certain components that are not biologically degradable, which distinguishes it from the BOD test; therefore, COD values are generally higher than BOD values

(URL-4, 2025). Analyses of samples collected in the field will be performed in the laboratory according to the SM 5220 B method.

Total Coliform

All standard methods applied for the detection and enumeration of total coliforms and Escherichia coli in microbiological water analyses focus on identifying the coliform group of microorganisms (URL-5, 2025). Analyses will be conducted according to the TS EN ISO 9308-1 standard.

RESULTS AND DISCUSSION

This section presents the results of analyses conducted based on bacteriological and physicochemical data collected from the Karasu River. The data were compared across five stations, with detailed examinations of seasonal variations and pollution sources. The findings were evaluated in terms of both bacteriological and physicochemical parameters. Table 1 displays the measurements of pH, temperature, dissolved oxygen, conductivity, salinity, total dissolved solids, biochemical oxygen demand, chemical oxygen demand, and total coliform at five distinct points during the spring season. Table 2 presents the same parameters measured at the same locations during the autumn season.

Parameters such as pH, temperature, dissolved oxygen, conductivity, salinity, and total dissolved solids were measured instantaneously and on-site using the Multi 340i/SET WTW device, while biochemical oxygen demand, chemical oxygen demand, and total coliform analyses were performed in the laboratory after transporting samples in an iced thermos.

Additionally, this section explains the impacts of the identified pollution sources and their reflections on the overall ecosystem.

Table 1. *Results of Spring Term*

Parameter	pH	Temp.	Dissolved Oxygen		Conductivity	Salinity	TDS	BOD	COD	Total Coliform
Unit	-	^{0}C	mg/l	%	µS/cm	%	mg/l	mg/l	mg/l	KOB/ 100ml
Before Vasgirt Creek	8,30	15,3	7,19	84,6	396	0	269,28	11,6	32	$12x10^2$
After Vasgirt Creek	8,20	14	7,43	83,36	404	0	274,72	< 3	< 10	$72x10^1$
Tarla Region	8,31	13,8	6,2	67,5	401	0	272,68	< 3	< 10	$13x10^2$
Pre-Confluence Point of the WWTP Discharge Water Channel	8,43	14,1	7,77	86,3	420	0	285,6	< 3	< 10	$11x10^2$
Post-Confluence Point of the WWTP Discharge Water Channel	8,26	14,6	8,76	99,3	498	0	338,64	< 3	< 10	$30x10^2$

Table 2. Results of The Autumn Term

Parameter	pH	Temp.	Dissolved Oxygen		Conductivity	Salinity	TDS	BOD	COD	Total Coliform
Unit	-	^{0}C	mg/l	%	µS/cm	%	mg/l	mg/l	mg/l	KOB/ 100ml
Before Vasgirt	8,50	18,0	8,35	99,9	563	0	382,84	< 3	< 10	80
Creek	8,35	16,8	7,36	87,5	564	0	383,52	< 3	< 10	36
After Vasgirt Creek	8,36	16,6	8,25	92,6	589	0	400,52	< 3	< 10	50
Tarla Region	8,48	16,8	8,16	97,0	569	0	386,92	< 3	< 10	$11x10^1$
Pre-Confluence Point of the WWTP Discharge Water Channel	8,20	17,7	7,95	98,6	660	0	448,80	13,6	37,3	$85x10^3$

pH

The pH values of all water samples collected from five points along the Karasu River were found to be slightly alkaline. Among the five points sampled in the spring period, the lowest pH measurement was recorded at the point downstream of Vasgirt Stream, with a value of 8.20. Vasgirt Stream flows roughly through the western part of Erzincan city center and has a relatively low flow rate. In the autumn period, the lowest pH was observed at the point downstream of the wastewater treatment plant (WWTP) discharge channel, also measuring 8.20. This water channel serves agricultural irrigation purposes and passes through many parts of the city. The WWTP discharge enters this channel, which joins the Karasu River approximately 5.5 km west of the treatment plant.

The highest pH value during the spring period, 8.43, was recorded just upstream of the WWTP discharge channel. In the autumn period, the highest pH value of 8.50 was measured upstream of Vasgirt Stream.

Comparing these pH values indicates no significant seasonal variation between spring and autumn measurements. The high flow rate of the Karasu River helps stabilize the pH values. Seasonal comparison also suggests a slight increase in average pH.

Temperature

During spring measurements, the lowest temperature was recorded in the agricultural field area at 13.8°C, while the highest temperature was 15.3°C, measured upstream of Vasgirt Stream. In the autumn, the lowest temperature was 16.6°C at the field site, and the highest was 18.0°C upstream of Vasgirt Stream.

Seasonal averages indicate cooling of waters in spring (post-winter) and warming in autumn (post-summer).

Dissolved Oxygen (DO)

The lowest dissolved oxygen level in spring was 6.2 mg/L (67.5%) at the field site, likely influenced by nutrient runoff from fertilization activities. The highest value was 8.76 mg/L (99.3%) downstream of the WWTP discharge channel.

In autumn, the lowest DO was 7.36 mg/L (87.5%) at the field site, and the highest was 8.35 mg/L (99.9%) upstream of Vasgirt Stream. The high DO at this latter point may indicate minimal impact from urban runoff within Erzincan city center.

Overall, a slight seasonal increase in dissolved oxygen concentration was observed.

Electrical Conductivity

In spring, the lowest electrical conductivity was 396 µS/cm upstream of Vasgirt Stream, and the highest was 498 µS/cm downstream of the WWTP discharge channel. In autumn, values ranged from 563 µS/cm (lowest, Vasgirt Stream upstream) to 660 µS/cm (highest, WWTP discharge downstream).

Seasonal comparison reveals an increase in conductivity during the autumn period.

Salinity

Salinity was measured as zero across all sampling points in both spring and autumn, showing no seasonal change.

Total Dissolved Solids (TDS)

Spring measurements showed the lowest TDS at 269.28 mg/L upstream of Vasgirt Stream and the highest at 338.64 mg/L downstream of the

WWTP discharge channel. In autumn, the lowest TDS was 382.84 mg/L (Vasgirt Stream upstream) and the highest 448.80 mg/L (WWTP discharge downstream).

TDS values correspond proportionally with conductivity, with higher values in autumn compared to spring.

Biological Oxygen Demand (BOD)

In spring, BOD was measured at 11.6 mg/L only upstream of Vasgirt Stream; other points showed BOD values below 3 mg/L, reported as <3 mg/L by the accredited laboratory, without exact quantification. In autumn, BOD was only elevated downstream of the WWTP discharge channel at 13.6 mg/L, while other points remained below 3 mg/L.

Chemical Oxygen Demand (COD)

Similarly, COD values in spring were only elevated upstream of Vasgirt Stream at 32 mg/L, with other locations below 10 mg/L (<10 mg/L reported). In autumn, the only elevated COD was downstream of the WWTP discharge at 37.3 mg/L, others remained below 10 mg/L.

Total Coliform

Spring total coliform counts ranged from the lowest 72×10^1 CFU/100 ml downstream of Vasgirt Stream to the highest 30×10^2 CFU/100 ml downstream of the WWTP discharge channel. Autumn values showed an increase, with the lowest 36 CFU/100 ml at Vasgirt Stream downstream and the highest 85×10^3 CFU/100 ml downstream of the WWTP discharge.

There was a notable seasonal increase in total coliform bacteria.

General Observations

Slight increases in dissolved oxygen, conductivity, and TDS were observed before and after Vasgirt Stream, likely due to increased flow from precipitation and tributary input into the Karasu River.

The field site exhibited the lowest dissolved oxygen in spring due to intensive fertilization but showed improved values in autumn, probably from melting snow increasing river discharge and oxygen levels.

BOD and COD levels remained relatively stable, but total coliform bacteria increased significantly, possibly due to enhanced bacterial activity during the summer months.

Comparison with Previous Studies and Regulations

No previous bacteriological or physicochemical pollution studies on the Karasu River within Erzincan province are available for direct comparison. However, a related study conducted on 11 sampling points along the Karasu River in Erzurum (Oğuz, 1997) examined similar parameters: dissolved oxygen, BOD, and COD. That study found dissolved oxygen levels between 4-5 mg/L, BOD between 12-13 mg/L, and COD between 19-20 mg/L.

The Karasu River, flowing through Erzurum and Erzincan provinces, is one of two main tributaries forming the Fırat River in Elazığ. Our study differs by focusing on pollution in Erzincan's central section through selected sampling points.

Compared to previous findings, dissolved oxygen increases, while BOD and COD decrease downstream in Erzincan, illustrating a spatial variation along the river.

Water Quality Assessment According to National Regulations

According to the "Surface Water Quality Regulation" effective since 30.11.2012 (Official Gazette No. 28483), which replaced certain provisions of the earlier Water Pollution Control Regulation (31.12.2004, Official Gazette No. 25687), water quality is classified based on biological, chemical, physicochemical, and hydromorphological criteria.

Using parameters measured at the five points (pH, conductivity, dissolved oxygen, COD, and BOD), the water quality of the Karasu River in Erzincan city center was evaluated:

pH values (8.20–8.50) fall within Class 1 in the water quality table.

Dissolved oxygen (6.2–8.35 mg/L) corresponds to Class 2.

BOD values (2–13.6 mg/L) fall into Class 3.

COD values (9–37.3 mg/L) correspond to Class 1.

Considering these four parameters together, the overall water quality of the Karasu River in the Erzincan city center section is classified as Class 3 (moderate quality) according to the Surface Water Quality Regulation.

RESULTS AND DISCUSSION

In this study, the bacteriological and physicochemical pollution of water samples taken from five points of the Karasu River were examined.

Since the Karasu River has a high flow rate, it has a strong potential to reduce the pollution it carries. Therefore, no significant fluctuations were observed in the measured parameters. However, the river passes through multiple cities and is exposed to considerable pollution.

Especially in the agricultural areas, intensive fertilization activities have some impact on the river, but after the melting of snow waters, the river eliminates this pollution over the long term. On the other hand, the direct discharge of domestic waste and industrial effluents into the Karasu River through the open drainage channels, which drain excess water from agricultural lands and are all connected to this stream, causes the river to face a serious pollution problem.

In the future, it appears essential that water discharges into the Karasu River be treated in wastewater treatment plants before being released.

A study conducted in Erzurum in 1997 (Oğuz, 1997) classified the water quality of the Karasu River as Class 3. Similarly, based on field sampling results in 2024, it was found that the Karasu River water quality falls under Class 3 for four parameters. According to the Surface Water Quality Regulation, Class 3 water is classified as polluted water. The fact that the water body studied is of Class 3 quality also indicates a "Moderate" water status. According to the same regulation, Class 3 water refers to water suitable for aquaculture and industrial use after appropriate treatment, except for facilities requiring high-quality water such as food and textile industries.

The pollution detection at some points (9 parameters at 5 points) of the Karasu River water body was limited due to budget constraints of the study, preventing an increase in the number of parameters to be analyzed. It is considered that allocating a larger budget to such studies would make it possible to more accurately determine and classify the water quality of surface waters.

Acknowledgements: This study was supported by Munzur University Scientific Research Projects Unit under the master's project number **YLMU024-04.**

References

Ács, É., Reskóné, N. M., Szabó, K., Taba, G., & Kiss, K. T. 2005. Application of epiphytic diatoms in water quality monitoring of Lake Velence-recommendations and assignments. Acta Botanica Hungarica, 47(3-4), 211-223.

Aras, S., Findik, O., Kalipci, E., & Sahinkaya, S. 2017. Assessment of concentration physicochemical parameters and heavy metals in Kızılırmak River, Turkey. Desalination and Water Treatment, 72, 328-334.

Atabay, N., E. Çetin, H. İnan, G. Yılmaz. 1995. Evsel Atıksulardan Bardenpho Prosesi ile Azot ve Fosfor Giderimi. Çevre Sempozyumu, 18-20 Eylül, Erzurum, 72-79.

Baştürk, E., & Alver, A. 2019. MELENDİZ NEHRİ SU KALİTESİNİN FARKLI KULLANIM AMAÇLARINA GÖRE DEĞERLENDİRİLMESİ. Niğde Ömer Halisdemir Üniversitesi Mühendislik Bilimleri Dergisi, 8(2), 731-740.

Bauchard, D.C., M.K. Williams, R.Y. Surampalli. 1992. Nitrate Contamination of Groundwater: Sources and Potential Health Effect. Journal AWWA, 84(9): 85-90.

Bilgin, A. 2015. An assessment of water quality in the Coruh Basin (Turkey) using multivariate statistical techniques. Environmental Monitoring and Assessment, 187(11), 721.

Bulut, C., Akçimen, U., Küçükkara, R., Savaşer, S., Uysal, K., KÖSE, E., & TOKATLI, C. 2012. ALABALIK ÜRETİMİ YAPILAN AKPINAR DERESİ (DENİZLİ) SU KALİTESİNİN DEĞERLENDİRİLMESİ. Anadolu University of Sciences & Technology-C: Life Sciences & Biotechnology, 2(2).

Çankaya, Ş., Varol, M., & Bekleyen, A. 2023. Hydrochemistry, water quality and health risk assessment of streams in Bismil plain, an important agricultural area in southeast Türkiye. *Environmental Pollution*, *331*, 121874.

Çelekli, A., Lekesiz, Ö., Yavuzatmaca, M., & Dügel, M. 2024. Fuzzy logic as a novel approach to predict biological condition gradient of various streams in Ceyhan River Basin (Turkey). *Science of The Total Environment*, *916*, 170069.

Guo-chen, L. I., Lu-san, L. I. U., Xing, W., & Li, L. I. 2012. Applications of diatom in river health assessment: A review. Yingyong Shengtai Xuebao, 23(9).

Hosmani, S. P. 2012. Application of benthic diatom community in lake water quality monitoring.

Hwang, S.-J., Kim, N.-Y., Won, D. H., An, K. K., Lee, J. K., & Kim, C. S. 2006. Biological assessment of water quality by using epilithic diatoms in major river systems (Geum, Youngsan, Seomjin River), Korea. Journal of Korean Society on Water Environment, 22(5), 784-795.

Kalyoncu, H., & Serbetci, B. 2013. Applicability of diatom-based water quality assessment indices in Dari stream, Isparta-Turkey. Proceedings of World Academy of Science, Engineering and Technology, 78, 1873.

Köse, E., Emiroğlu, Ö., Çiçek, A., Aksu, S., Başkurt, S., Tokatli, C., Şahin, M., & Uğurluoğlu, A. 2020. Assessment of Ecologic Quality in Terms of Heavy Metal Concentrations in Sediment and Fish on Sakarya River and Dam Lakes, Turkey. Soil and Sediment Contamination: An International Journal, 29(3), 292-303.

Kutlu, B., Sesli, A., Tepe, R., & Mutlu, E. 2015. Assessment of physico-chemical water quality of birecik dam, Şanlıurfa, west east region, turkey. Turkish Journal of Agriculture-Food Science and Technology, 3(7), 623-628. http://www.agrifoodscience.com/index.php/TURJAF/article/view/423

Noga, T., Stanek-Tarkowska, J., Pajączek, A., Peszek, Ł., & Kochman, N. 2013. Ecological characterization of diatom communities in the Wisłok River with application of their indicatory role to the evaluation of water quality. Journal of Ecological Engineering, 14(4).

Oğuz E., 1997. Erzurum Kara Nehri Kirlilik Parametrelerinin Matematik Modellemesi.

Ormerod K., et al. 1982. Bacteriological Examination. MJ Suess Ed., Pergamon Press, Oxford.

Oskay, V., Karagöz, Ö., & Kuşlu, S. 2023. Investigation of the water quality of Aktutan pond located in Gümüşhane province in the North East region of Turkey by Hazen statistical method. Environmental Earth Sciences, 82(5), 118.

Ram, N.M., R.F.F. Christman, K.P. Cantor. 1990. Significance and Treatment of Volatile Organic Compounds in Water Supplies. Library of Congress Cataloging-Publication Data.

Shen, R., Ren, H., Yu, P., You, Q., Pang, W., & Wang, Q. 2018. Benthic diatoms of the Ying River (Huaihe River Basin, China) and their application in water trophic status assessment. Water, 10(8), 1013.

Szczepocka, E., Szulc, B., Szulc, K., Rakowska, B., & Żelazna-Wieczorek, J. 2014. Diatom indices in the biological assessment of the water quality based on the example of a small lowland river. Oceanological and Hydrobiological Studies, 43(3), 265-273.

Tokatlı, C., Solak, C. N., & Yılmaz, E. 2020. Water quality assessment by means of bio-indication: A case study of ergene river using biological diatom index. *Aquatic Sciences and Engineering*, *35*(2), 43-51.

Tokatlı, C., Solak, C. N., Yılmaz, E., Atıcı, T., & Dayıoğlu, H. 2020. Research into the epipelic diatoms of the Meriç and Tunca Rivers and the application of the biological diatom index in water quality assessment. *Aquatic Sciences and Engineering*, *35*(1), 19-26.

Tuncel M., 2024. İslam Ansiklopedisi.

Ubay, G., D. Kantarcı, C. Bayat, A. Hacıhanefioğlu. 1995. Yerleşim Alanlarında Evsel Nitelikli Arıtma Tesislerinden Çıkan Arıtılmış Suların Yeşil Alanlarda Yeniden Kullanılabilirliliğinin İncelenmesi. İstanbul Üniv. Araştırma Fonu Projesi, I: Gelişme Raporu.

URL-1,2024. https://megep.meb.gov.tr/mte_program_modul/moduller_pdf/Sularda%20Fiziksel%20Analizler.pdf

URL-2, 2024. https://www.mgm.gov.tr/genel/hidrometeoroloji.aspx?s=3. 01.Nisan.2024

URL-3, 2025. https://cevre.wordpress.com/wp-content/uploads/2008/12/biyolojik-oksijen-ihtiyaci-analiz-yontemi.pdf

URL-4, 2025. https://www.laboratuvar.net/gida-analizleri/kimyasal-analizler/kimyasal-oksijen-ihtiyaci-koi-tayini

URL-5, 2025. https://www.diatek.com.tr/Makale-Yontem/Sularda-Koliform-Grubu-Bakteri-Analizleri/Sularda-Koliform-Grubu-Bakteri-Analizleri_134.html

Venkatachalapathy, R., & Karthikeyan, P. 2015. Application of Diatom-Based Indices for Monitoring Environmental Quality of Riverine Ecosystems: A Review. Içinde Mu. Ramkumar, K. Kumaraswamy, & R. Mohanraj (Ed.), Environmental Management of River Basin Ecosystems (ss. 593-619). Springer International Publishing.

Vincent W.F., Effects of climate change on lakes. In Encyclopedia of Inland Waters (Ed. G.E. Likens) 3 (2009): 55-60.

Xue, H., Wang, L., Zhang, L., Wang, Y., Meng, F., & Xu, M. 2023. Exploration of Applicability of Diatom Indices to Evaluate Water Ecosystem Quality in Tangwang River in Northeast China. *Water*, *15*(20), 3695.

Yılmaz, E., Koç, C., & Gerasimov, I. 2020. A study on the evaluation of the water quality status for the Büyük Menderes River, Turkey. Sustainable Water Resources Management, 6(6), 100.

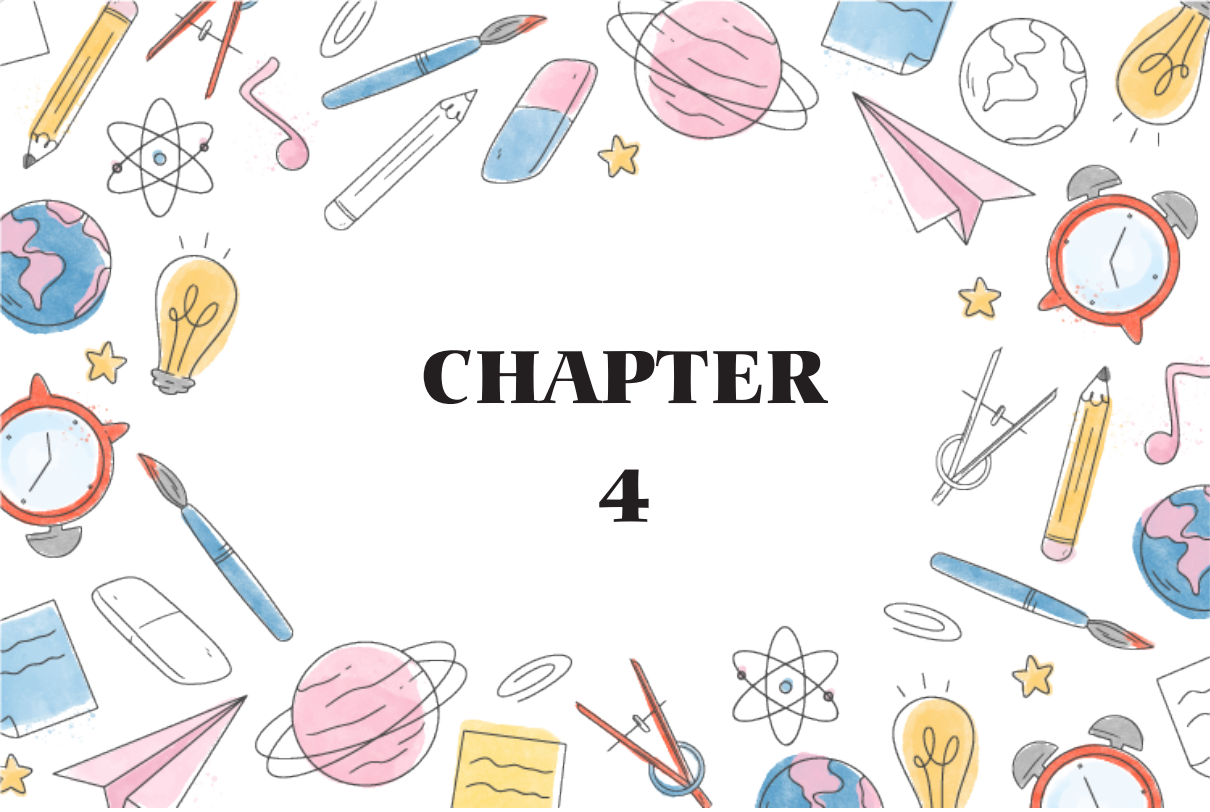

CHAPTER 4

SIMULTANEOUS DESIGN OF ACTIVELY MORPHING SWEPT ANHEDRAL BLADE TIP AND ROTORCRAFT FLIGHT CONTROL-SYSTEM

Fırat ŞAL[1]

1 Faculy of Aeronautics and Astronautics, Iskenderun Technical University, Iskenderun/Hatay, 31215, Turkey, firat.sal@iste.edu.tr

Orcid No: https://orcid.org/0000-0003-2412-4131

1. Introduction

Substantial developments and progresses for rotorcraft flight control systems (i.e., RFCSs) in order to decrease energy have been done by applying re-design/simultaneous design approach over last years. Some of these re-design approaches on rotorcraft are applying moving horizontal tailplane (see articles [1] to [6] for different implementations). Some of different approaches are redesigning the rotorcraft blade features such as radius and chord before starting the flight called as passive morphing in the appropriate expertise or continuously varying different rotorcraft blade features such as radius and twist during the flight called as active morphing in the appropriate expertise. For instance, in [7] passive morphing was fairly beneficial for decreasing the energy of specific rotorcraft. In that paper, some of the passively morphing features were blade radius and linear mass density. Around 33% of energy of RFCS at 40 kts straight-level flight (i.e., SLF) situation is saved. Additionally, in [8] active morphing was considerably helpful for reducing the energy of previously mentioned same rotorcraft, and some of the actively morphing features were blade radius and twist. Using previously mentioned new active morphing approach around 85% of the energy of RFCS at 40 kts SLF situation is saved (visit also other redesign research articles such as [9] to [19] for different redesign applications in passive and/or active cases).

Several investigations have been done for rotorcraft main rotor tip swept and anhedral considering dissimilar aims lately in the relevant area and these two parameters are main focus of this research article in active case. For instance, in [20] swept anhedral rotorcraft blade tip was researched in order to recover rotorcraft performance throughout SLF situation. In that paper aerodynamic and acoustic consequences were found. Consequently, a decrease of almost %7 on power necessary to drive rotorcraft rotor for hover was obtained. In addition, a noise decrease of 1 dB was obtained using swept anhedral geometry in that article. Furthermore, in another research article [21] for optimizing the aerodynamic performance of an unmanned aerial vehicle, swept anhedral geometry was evaluated. Tip swept was benefitted in

order to avoid compressibility effects in SLF situation. Additionally, tip anhedral was benefitted for changing pitching moment which contributes decreasing control loads. From aerodynamic aspect, use of swept anhedral tip geometry was obtained so beneficial. Additionally, in another review article in [22] rotorcraft tip geometry design capturing swept anhedral geometry in order to estimate the routine of novel tip geometries was evaluated. In that paper it was obtained that applying swept anhedral geometry is fairly beneficial from the aspects of aerodynamics, structure and acoustic. Moreover, in another study in [23] a new method for obtaining blade features capturing tip swept and tip anhedral during recovering aerodynamic routine was established in hover and dissimilar SLF situations. In that paper by applying swept anhedral tip geometry substantial development in aerodynamic routine was obtained (see also research papers such as [24] to [29] for several swept and/or anhedral tip geometry examples).

Numerous control techniques for RFCSs have been used recently in the relevant literature. OVCs are (visit [30] for more details) applied for our RFCS. These kinds of control-systems have various superiorities. Initially, OVCs are modified LQG control-systems and OVCs capture Kalman filters inside. Second, OVCs contribute second-order information (visit [31] and [32] for details).

In this research article rather than using passive morphing, active morphing is chosen. Passive morphing just permits the rotorcraft design features to be attuned before starting the flight. It is not possible to vary any of these features (e.g. main rotor blade radius, main rotor angular velocity, etc.), or certainly the RFCS parameters, when the flight is started. However, active morphing permits for the continuous variation of specific features all over the flight. Active morphing necessitates unceasing measurements and actuation and also demands some kind of feedback control-system mechanism (see [33] for additional discussion in this consideration). In this research article, the main innovation of the research is explained next: the possibility of AMSA blade tip is investigated for first time in the relevant expertise in order to save

more energy than possible in the passive morphing situation. For this purpose simultaneous AMSA blade tip and RFCS design is also first time considered in the relevant expertise by regarding previously mentioned aim. Lastly, for the relevant simultaneous design approach SPSA is also first time benefitted in the relevant expertise. In addition, closed loop responses' (i.e., CLRs) evaluations by applying OVCs between rotorcraft (i.e., AMSA blade tip having ones and not having ones) is also first time examined. Here it is obtained that applying simultaneous design methodology for AMSA blade tip and RFCS reasons less energy than the ones not having this strategy. Additionally, this causes less energy waste and clean environment. Here, first used rotorcraft models and used blade tip variables are mentioned. Then, used RFCS and used optimization technique for simultaneous design are shared. Final, effects of AMSA blade tip on energy and as well as CLRs are shared. The morphing is achieved during operation of the rotor blade in flight in this research paper.

1. Used Rotorcraft Blade Design Variables

Here blade tip swept angle and anhedral are included to previously mentioned rotorcraft models in actively morphing case. The morphing is achieved during operation of the rotor blade in flight. In Figure 1 rotorcraft blade tip swept and anhedral are shared, respectively. Here, the results of application of them in actively morphing case are evaluated while minimizing energy of RFCS. These 2 terms are blade redesign variables in this research article.

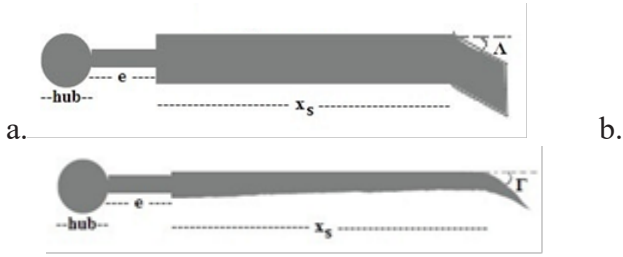

Figure 1 Sketch of swept and anhedral
(a) From top (b) From side
(where Λ: swept angle, Γ: anhedral angle)

For composing rotorcraft dynamical models all of the effects mentioned above were assembled into the nonlinear equations of the rotorcraft dynamics by using Maple software and they are found in the generic implicit form as below:

$$f(\dot{x}, x, u) = 0 \qquad (1)$$

where $f \in \mathbb{R}^{28}$, $x \in \mathbb{R}^{25}$ is the nonlinear state vector capturing the 9 body states (i.e. 3 linear velocity states, 3 angular velocity states, 3 Euler angle states) and blade states (i.e.4 flapping states and 4 lead-lagging states) , and $u \in \mathbb{R}^{4}$ is the nonlinear control vector including 2 cyclic controls and 1 collective control for the main rotor and 1 tail rotor control. For the design of flight control system, the previously mentioned rotorcraft nonlinear models are linearized around several forward flight trim conditions.

2. Used RFCS

For RFCS here OVC is selected. A thorough examination of OVCs and its advantages can be reached in [31] and [32]. A short explanation will also be given in this section next:

For a supposed continuous, LTI, stabilizable, and detectable system, as well as a positive definite input penalty matrix, obtain a full-order dynamic controller:

$$\min_{A_c,F,G} \; J = E_\infty \; u_p^T R u_p = tr(RGX_{c_j} G^T)$$

(2)

face to face bounds on the outputs

$$E_\infty \; y_i^2 \le \sigma_i^2, \qquad i = 1,....,n_y$$

(3)

General structure of OVC is shared in Figure 2, where the left side proposes a linear model while the right side proposes a full-order dynamic controller.

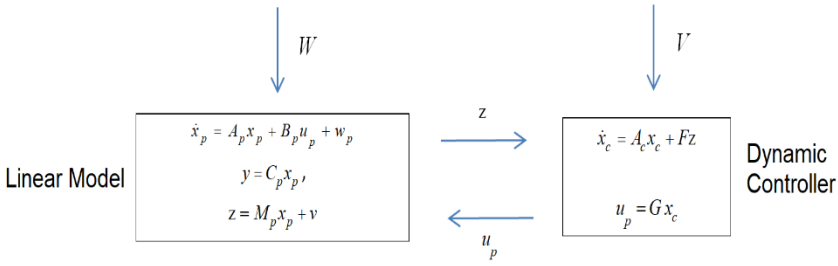

Figure 2 Illustration of OVC

Here an OVC is advised for RFCS while minimizing energy depending on both rotorcraft parameters and controller parameters.

3. Used Optimization Procedure

The simultaneous design challenge for AMSA tip and RFCS in order to minimize energy is given next:

$$\min_{A_c,F,G,\Psi_t} \; J = E_\infty \; u_p^T R u_p$$

(4)

face to face Equation (10) where $\Psi_t = \{\Lambda, \Gamma\}$. The variables of Ψ_t are bounded as following: $\Psi_{ti_{\min}} \le \Psi_{ti} \le \Psi_{ti_{\max}}$. Here the matrices of linear model A_p and B_p depend on Ψ_t, and relevant dependency spreads through energy computation (see Eq. 9) to J and to output variance values (see Eq. 10). These dependencies reason to a sophisticated optimization problem where both the objective, J, and the variance constraints depend on the optimization variables in a complicated manner. Here SPSA is applied and described next: It is inexpensive since it applies only two calculations of the objective to guess the gradient (visit [34] for more details).

4. Effect of AMSA Blade Tip on Energy of RFCS

Effects of AMSA blade tip on energy of the RFCS are investigated. Rotorcraft models (see references [6], [7], [8], [30] and [33]) are linearized around 80 kts SLF situation for this purpose here. For RFCS OVCs are benefitted by using bounds on attitude angles (i.e., 10^{-4} for each of them) while inputs are whole of traditional rotorcraft controls) and also AMSA blade tip angles. Here for swept and anhedral, primary trim amounts are 20 degrees. Additionally, it begins at %75 of the blade radius. The low and up bounds for blade tip variables in this application are lower={10 degrees, 10 degrees, %70*R} and upper={30degrees, 30 degrees, %90*R}, respectively. Actually, the power associated with the perturbation control actuation is minimized here. In Figure 3, energy minimization for AMSA tip is shown. Furthermore, optimum values for design features are Λ_t=20.1018 degrees (trim value of swept angle), Γ_t=19.8968 degrees (trim value of anhedral angle), xs=%71.46*R. Here the relative energy saving is defined as well and it is defined next: $\%J = 100(J_n - J_m)/J_n$ where J_n and J_m are nominal and minimized energies of RFCSs. The energy is applied here for the situations of AMSA tip non-used rotorcraft (i.e., traditional rotorcraft) and AMSA tip used rotorcraft at any iteration of SPSA (i.e., any modified rotorcraft). The energy is also used here for the situation of AMSA tip used rotorcraft at final iteration of SPSA (i.e., final modified rotorcraft). The relative energy savings between initial modified rotorcraft and any

modified rotorcraft are shared in Figure 4. It can be realized that after application of simultaneous AMSA blade tip and RFCS design %J is approximately 21.6. Additionally, the relative energy save between traditional rotorcraft and final modified rotorcraft (i.e., owing Λ_t=20.1018 degrees, Γ_t=19.8968 degrees, and xs=%71.46*R) is approximately %J=%85. Obtained amount also proves that benefitting initial modified rotorcraft is also cheaper than benefitting traditional rotorcraft from the aspect of energy.

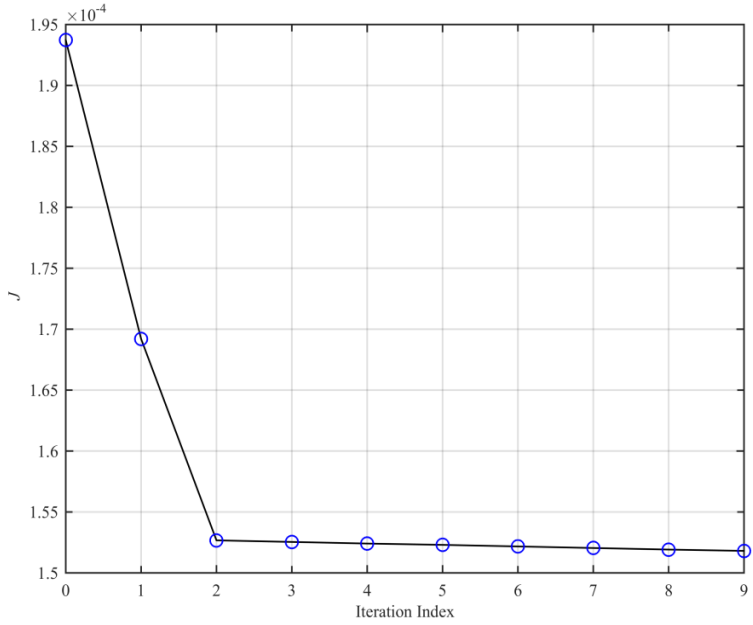

Figure 3 Energy minimization for AMSA blade tip

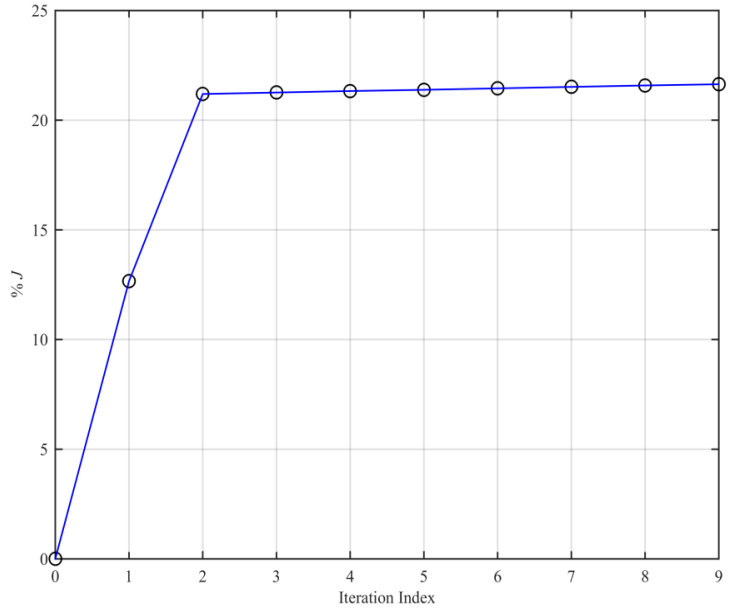

Figure 4 Relative energy save for AMSA blade tip

5. Effect of AMSA Blade Tip on CLRs

Here after benefitting simultaneous AMSA blade tip and RFCS design, CLR analysis is done for the situations of non-used AMSA tip and used AMSA tip, respectively. For relevant situations, a closed-loop system (i.e, CLS) is found through integration of our traditional rotorcraft (i.e., Puma SA 330) and an OVC designed for this nominal system first. For the second situation, additional CLS is found by integrating initial modified rotorcraft (i.e., having initial value of the AMSA blade tip) having initial AMSA tip and OVC designed for this initial modified system. For the last situation, another CLS is found by integrating final modified rotorcraft having optimum AMSA tip and OVC designed for final modified system. The figure variables are represented in degrees to demonstrate their behaviors in a superior quality below. It is also vital to say that because linearized models

are benefitted here, the real values of the figure parameters differ from their trim values in the figures. In addition, the CLSs are entirely affected by Gaussian white noises.

In Figure 5 the CLRs for outputs of interets are shown. It can be detected from Figure 5 that the qualitative and quantitative behaviors of attitude angles are fundamentally the same for entire of the three rotorcraft since the expected values ($E_\infty\ y_i^2$) for the outputs of interest are very close and follow the bounds on them ($E_\infty\ y_i^2 \le \sigma_i^2$).

In Figure 6 CLRs for inputs of interest are given for entire rotorcraft types. The significant comment about CLRs is that commonly the peak values are the largest for the 1st CLS. This comment occurs since the energy of OVCs for the associated CLSs are *J*=11.4*10^-4, *J*_i=1.94*10^-4 and *J*_f=1.52*10^-4, respectively. Additionally, the control input deviances are smooth and small, and also do not demonstrate any catastrophic behavior. It is as well as essential to be noted that for dissimilar flight situations such as hover and 40 kts SLF condition, the formerly obtained consequences are again valid.

In Figure 7 CLRs of some other rotorcraft states such as longitudinal and vertical linear velocities and lateral angular velocity are given. It shows that the other rotorcraft outputs such as *u* and *w* do not experience catastrophic characteristics. Additionally, for entire of rotorcraft variants (i.e. traditional rotorcraft, initial modified rotrocraft and final modified rotorcraft), the qualitative behaviors are almost the same.

In Figure 8 CLRs of other rotorcraft main rotor states (i.e., collective main rotor blade flapping, longitudinal blade flapping, collective blade main rotor lead-lagging, and longitudinal blade lead-lagging) are shared for entire of rotorcraft variants. It proves that the other rotorcraft main rotor outputs do not face to face catastrophic characteristics. Additionally, entire of rotorcraft types, qualitative behaviors are also still almost similar.

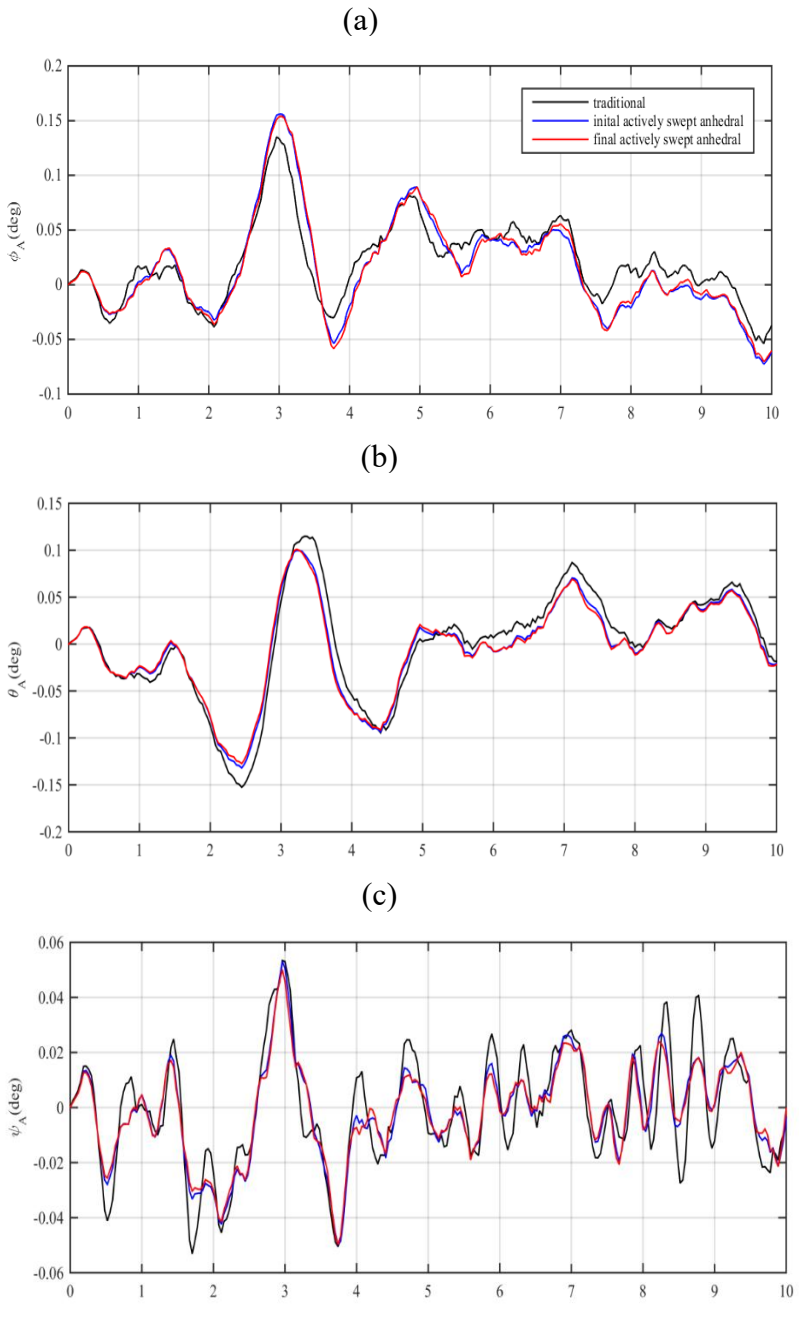

Figure 5 Effects on outputs of interest

(a)

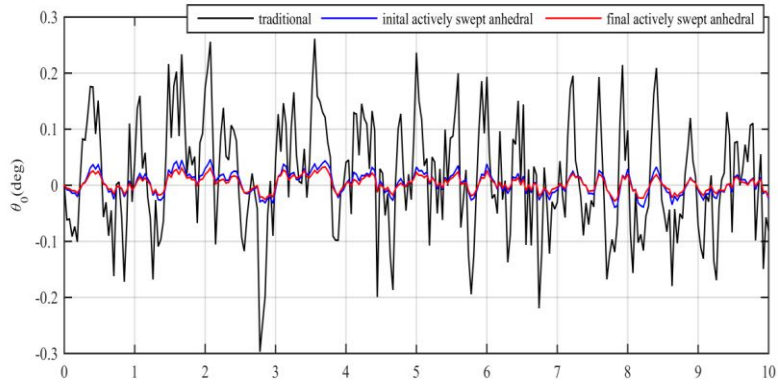
traditional
inital actively swept anhedral
final actively swept anhedral
θ_0(deg)

(b)

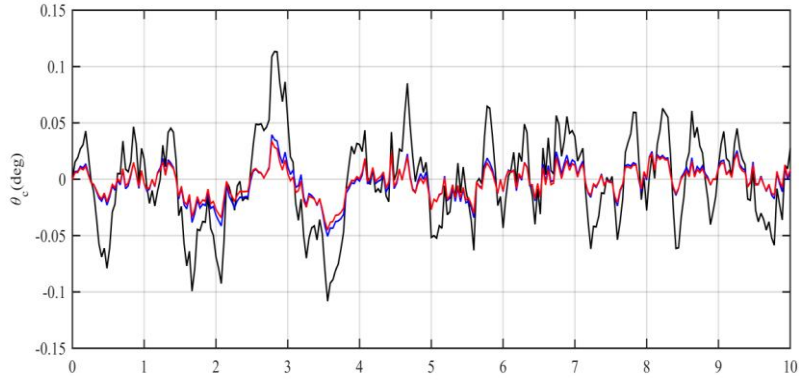
θ_c(deg)

(c)

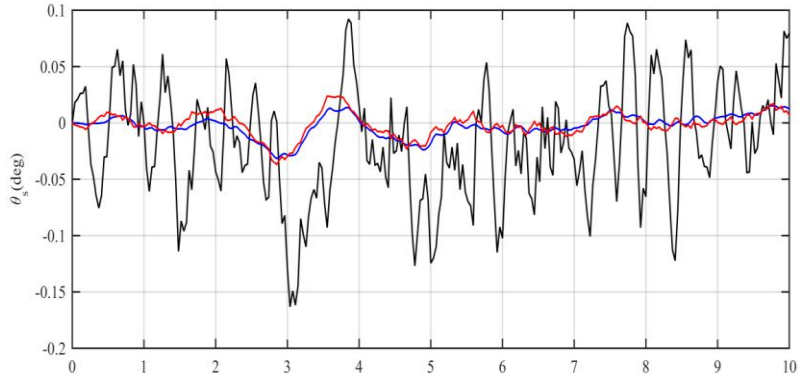
θ_s(deg)

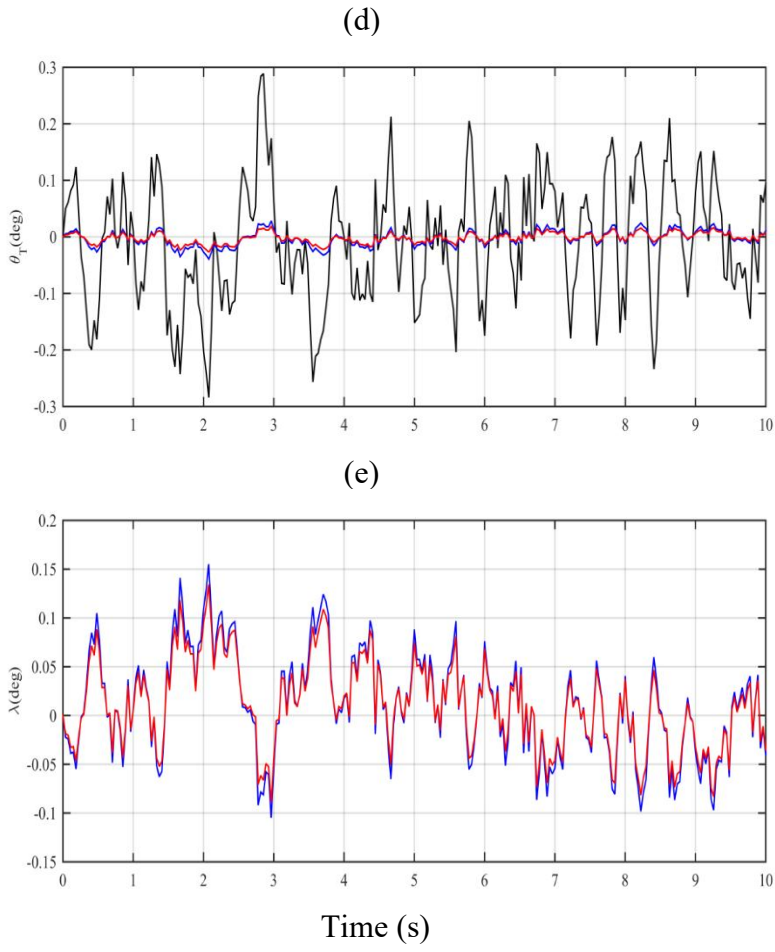

Figure 6 Effects on inputs of interest

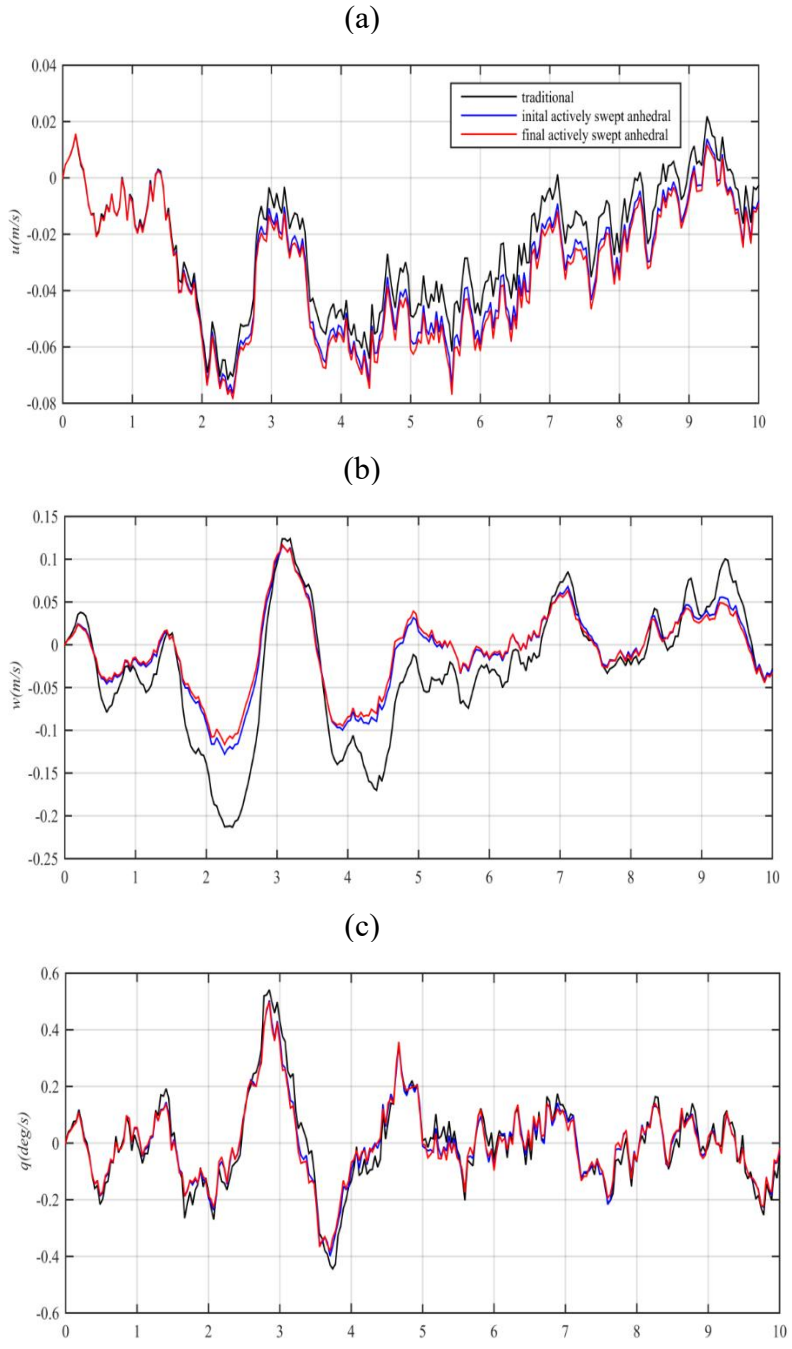

Figure 7 Effects on some other rotorcraft states

(a)

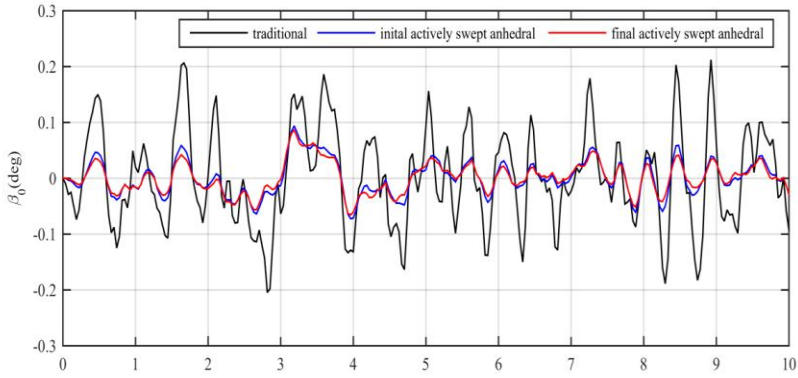
traditional
inital actively swept anhedral
final actively swept anhedral
β_0(deg)

(b)

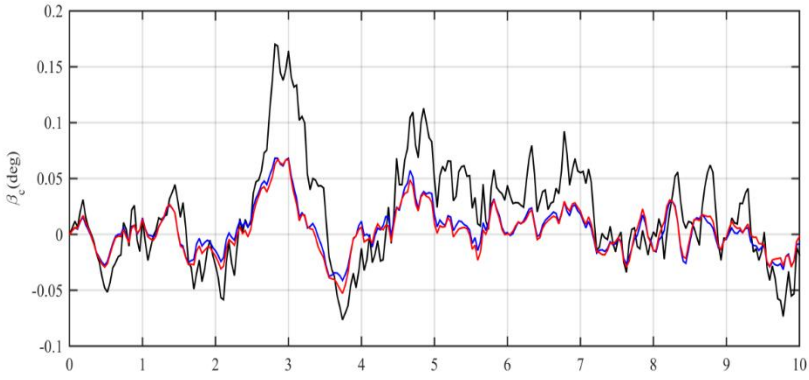
β_ζ(deg)

(c)

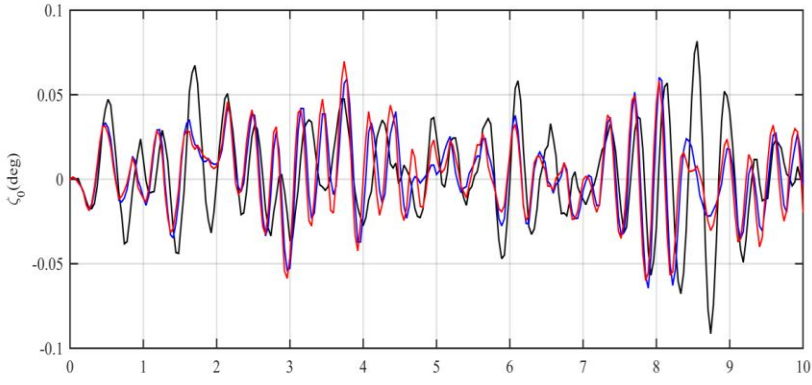
ζ_0(deg)

(d)

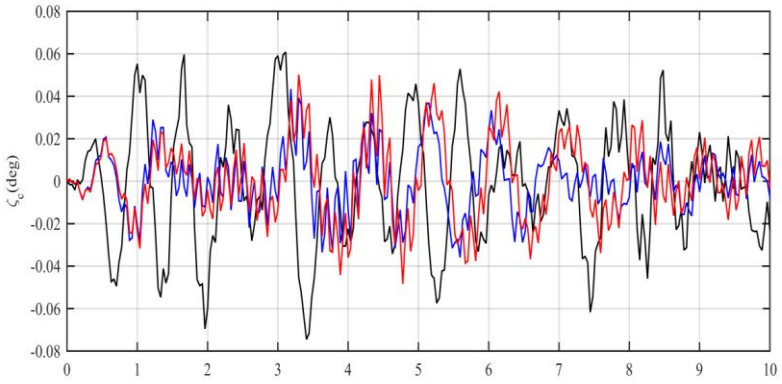

Figure 8 Effects on some main rotor states

6. Conclusions

Here, the consequences of using simultaneous actively morphing swept anhedral (i.e, AMSA) rotorcraft blade tip and rotorcraft flight control-system (RFCS) design on energy, and likewise on the related closed loop responses (i.e, CLRs), have been investigated. Three situations (i.e., a traditional rotorcraft controlled by an output variance constrained controller: OVC and two other modified rotorcraft having AMSA blade tip and controlled by a related OVC) were studied from the perspective of not only energy but also CLRs.

Concerning the original 'traditional' rotorcraft, the energy was obtained as almost J=11.4*10^-4 at 80 kts straight-level flight (i.e., SLF) situation. Moreover, for the modified rotorcraft having AMSA blade tip and controlled by related OVC, the energies were obtained as J_i=1.94*10^-4 and J_f=1.52*10^-4 for initial and final iterations, respectively while using SPSA as optimization tool. These values are the costs of the applied OVC control systems. The relative energy save is nearly %21.6 between initial modified (i.e., having initial value of the AMSA blade tip) and final modified AMSA blade tip having rotorcraft after using SPSA. Furthermore, the relative energy save between traditional

rotorcraft and final modified rotorcraft is nearly %85. This quantity as well as shows that benefitting initial modified rotorcraft is cheaper than benefitting traditional rotorcraft from the domain of energy.

Several vital consequences relevant with CLRs were also found. Firstly, since quantity of variance bounds on outputs of interest (i.e., rotorcraft attitude angles) are the same for all of CLSs (i.e., closed loop responses), the qualitative and quantitative behaviors of them are almost fundamentally the same. Additionally, the other rotorcraft and main rotor outputs (e.g., linear velocity states, angular velocity states, blade flapping states, and blade lead-lagging states) do not face to face catastrophic characteristics. Second, the peak values of the all control inputs are the biggest for the 1st CLS. As a final, entire of the results obtained for CLSs are also appropriate for dissimilar flight situations such as hover and 40 kts SLF situation.

7. References

[1] Sherry J 1953 Helicopter stabilizer, U.S. Patent 2,630,985, March 10.

[2] Stuart J 1961 Horizontal tail plane for helicopters, U.S. Patent 2,979,286.

[3] Howlett, J 1981 UH-60 Black Hawk engineering simulation program, NASA Contractor Report 166309.

[4] Bluman J E 2008 Reducing trailing edge flap deflection requirements in primary control with a moveable horizontal tail, M.S. thesis.

[5] Bluman J E and Gandhi F S 2011 Reducing trailing edge flap deflection requirements in primary control with a movable horizontal tail. *Journal of the American Helicopter Society*, 56 (3), doi: https://doi.org/10.4050/JAHS.56.032005.

[6] Oktay T and Sal F 2015 Helicopter control energy reduction using moving horizontal tail. *The Scientific World Journal: Aerospace Engineering*, doi: 10.1155/2015/523914.

[7] Oktay T and Sultan C 2013a Simultaneous helicopter and control-system design. *AIAA Journal of Aircraft*, 50 (3): 911-926, doi: https://doi.org/10.2514/1.C032043.

[8] Oktay T. and Sultan C 2014 Flight control energy saving via helicopter rotor active morphing. *AIAA Journal of Aircraft*, 51(6): 1784-1805, doi: https://doi.org/10.2514/1.C032494.

[9] Ganguli R 2002 Optimum design of a helicopter rotor for low vibration using aeroelastic analysis and response surface methods. *Journal of Sound and Vibration*, 258(2): 327–344, doi: https://doi.org/10.1006/jsvi.2002.5179.

[10] Fusato D and Celi R 2006 Multidisciplinary design optimization for aeromechanics and handling qualities. *Journal of*

Aircraft, 43(1):241–252, doi: https://doi.org/10.2514/1.7943.

[11] Sahasrabudhe V, Tischler M, Cheng R, Stumm A, and Lavin M 2007 Balancing CH-53K handling qualities and stability margin requirements in the presence of heavy external loads. Proceedings of the American Helicopter Society 63rd Forum, Virginia Beach, VA, USA.

[12] Kim K-C and Chopra I 1992 Aeroelastic Analysis of Swept, Anhedral, and Tapered Tip Rotor Blades. *Journal of the American Helicopter Society*, 37(1):15-30.

[13] Kang, H Saberi, H and Gandhi F 2010 Dynamic blade shape for improved helicopter rotor performance. *Journal of the American Helicopter Society*, 55(3), doi: https://doi.org/10.4050/JAHS.55.032008.

[14] Barbarino, S., Gandhi, F and Webster, S D 2011 Design of extendable chord sections for morphing helicopter rotor blades. *Journal of Intelligent Material Systems and Structures*, 22(9):891–905, doi: https://doi.org/10.1177/1045389X11414077.

[15] Vu N A, Lee J W, J I S 2013 Aerodynamic design optimization of helicopter rotor blades including airfoil shape for hover performance. *Chinese Journal of Aeronautics*, 26(1):1-8, 2013. doi: https://doi.org/10.1016/j.cja.2012.12.008.

[16] Kambampati S and Ganguli R 2016 Nonrotating beams isospectral to tapered rotating beams. *AIAA Journal*, 54(2):750-757, doi: https://doi.org/10.2514/1.J054126.

[17] Stalewski W and Zalewski W 2019 Performance improvement of helicopter rotors through blade redesigning. *Aircraft Engineering and Aerospace Technology*, 91(5):747-755.

[18] Shahmiri F Sargolzehi M and Ashtiani M A S 2019 Systematic evaluation of the helicopter rotor blades: design variables and interactions. *Aircraft Engineering and Aerospace Technology*, 92(2):264-270.

[19] Sal F 2020 Effects of the actively morphing root chord and taper on helicopter energy. *Aircraft Engineering and Aerospace Technology*, 92(2):264-270.

[20] Desopper A, Lafon P, Philippe J J and Onera J P 1987 Effect of an anhedral sweptback tip on the performance of a helicopter rotor. 13th European Rotorcraft Forum, Arles, France.

[21] Marques P, Maligno A, Dierks S, Penev V and Bachouche A 2013 The Jinn military Unmanned Helicopter Program: Rotor blade tip aerodynamics of the advanced technology demonstrator. *International Journal of Unmanned System Engineerin*g, 3(1):6-15.

[22] Brocklehurst A and Barakos G N 2013 A review of helicopter rotor blade tip shapes. *Progress in Aerospace Sciences*, 56: 35-74.

[23] Lütke B 2017 Dynamic Stall on a Pitching Double-Swept Rotor Blade Tip. PhD Dissertation, Technical University Munich.

[24] Bernardini G, Piccione A, Serafini J, and Gennaretti M 2016 Optimal Design and Acoustic Assessment of Low-Vibration Rotor Blades.

[25] Droandi G and Gibertini G 2015 Aerodynamic blade design with multi objective optimization for a tiltrotor aircraft. *Aircraft Engineering and Aerospace Technology*, 87(1):19-29.

[26] Marcel V, Daniel Y, and Morteza G 2022 Parametric study of small-scale rotors in axial descent. *Physics of Fluids*, 34.

[27] Lee Y B and Park J S 2023 Effect of Blade Tip Configurations on the Performance and Vibration of a Lift-Offset Coaxial Rotor, *Aerospace*, 10(2).

[28] Uluocak S, Percin M, Uzol O 2021 Experimental investigation of tip anhedral effects on the aerodynamics of a model helicopter rotor in hover. *Aerospace Science and*

Technology, 113.

[29] Afshari R and Karimian S M H 2023 A new blade tip geometry to improve aerodynamic performance and acoustic noise of helicopter blade in hovering flight. *Aerospace Science and Technology*, 135.

[30] Oktay T 2012 Constrained Control of Complex Helicopter Models. Virginia Tech, PhD Dissertation.

[31] Skelton R E and Sultan C 1997, Controllable tensegrity, A new class of smart structures. SPIE Intl. Symposium on Smart Structures and Materials, San Diego, CA.

[32] Skelton R E and Lorenzo M D 1985 Space structure control design by variance assignment. *Journal of Guidance, Control, and Dynamics*, 8(4): 454-462.

[33] Oktay T and Sultan C 2015 Comfortable helicopter flight via passive/active morphing. *IEEE Transactions on Aerospace and Electronic Systems*, 51:2876-2886, doi: 10.1109/TAES.2015.140488.

[34] Spall J 1992 Multivariate stochastic approximation using a simultaneous perturbation gradient approximation. *IEEE Transactions on Automatic Control*.